

Systems and Protocols for Quantum Metrology and Quantum Computation

A dissertation presented

by

Péter Kómár

to

The Department of Physics

in partial fulfillment of the requirements

for the degree of

Doctor of Philosophy

in the subject of

Physics

Harvard University

Cambridge, Massachusetts

September 2015

©2015 - Péter Kómár

All rights reserved.

Thesis advisor

Mikhail D. Lukin

Author

Péter Kómár

Systems and Protocols for Quantum Metrology and Quantum Computation

Abstract

Abstract about

- Quantum computation protocols
- and their use
- Quantum metrology protocols
- and their use
- systems capable of realizing them
- namely: optomechanical systems
- atomic systems

Contents

Title Page	i
Abstract	iii
Table of Contents	iv
List of Figures	vi
List of Tables	vii
Citations to Previously Published Work	viii
Acknowledgments	ix
Dedication	x
1 Introduction and Motivation	1
1.1 Overview and Structure	1
1.2 Optomechanical Systems	1
1.3 Atom-Cavity Systems	1
1.4 Rydberg Interactions	1
1.5 Quantum Repeaters	1
1.6 Atomic Clocks and Quantum Metrology	1
2 Single-photon nonlinearities in two-mode optomechanics	2
2.1 Introduction	2
2.2 Multimode optomechanics	5
2.3 Equal-time correlations	8
2.3.1 Average transmission and reflection	8
2.3.2 Intensity correlations	11
2.3.3 Absence of two-photon resonance at $\Delta = 0$	14
2.3.4 Finite temperature	16
2.4 Delayed coincidence and single phonon states	21
2.4.1 Driven mode	22
2.4.2 Heralded single phonon states	25
2.5 Reaching strong coupling	28
2.6 Conclusions	29

3	Optomechanical quantum information processing	31
3.1	Introduction	31
3.2	Model	33
3.3	Resonant strong-coupling optomechanics	34
3.4	An OM single-photon source	37
3.5	Single-phonon single-photon transistor	38
3.6	Phonon-phonon interactions	40
3.7	Conclusions	42
4	Heralded Quantum Gates with Integrated Error Detection in Optical Cavities	43
4.1	Introduction	43
5	Long-distance entanglement distribution using individual atoms in optical cavities	44
5.1	Introduction	44
6	Heisenberg-Limited Atom Clocks Based on Entangled Qubits	45
6.1	Introduction	45
7	A quantum network of clocks	46
7.1	Introduction	46
8	Entangling collective Rydberg excitations of remote atomic ensembles	47
8.1	Introduction	47
A	Appendices for Chapter 2	48
A.1	Derivation of reflected mode operator	48
A.2	Analytic model	49
B	Appendices for Chapter 3	52
B.1	Phonon nonlinearities	52
B.1.1	Model	52
B.1.2	Displaced frame	53
B.1.3	Hybridized modes	54
B.1.4	Adiabatic elimination of the cavity mode	56
B.1.5	Simple perturbation theory	57
B.1.6	Corrections	58
B.1.7	Numerical simulation	59
B.2	Phonon-phonon interactions	61
	Bibliography	64

List of Figures

2.1	Two-mode optomechanical system	5
2.2	Lower level diagram of 2+1 optomechanical system	7
2.3	Photon statistics in mode anti-symmetric mode, a	9
2.4	Photon statistics in mode symmetric mode, s	10
2.5	Photon statistics in the reflected mode, R	10
2.6	Illustration of dominant processes	13
2.7	Aggregate photon statistics of both modes	16
2.8	Temperature dependence of the relevant levels	17
2.9	Effect of non-zero temperature on photon statistics of mode a	17
2.10	Effect of non-zero temperature on photon statistics of mode s	18
2.11	Autocorrelation of mode a	24
2.12	Autocorrelation of mode s	26
2.13	Diagram with metastable subspace	27
3.1	Model of two resonators	33
3.2	Behavior of the coupled system	35
3.3	A single-phonon single-photon transistor	38
3.4	Controlled phase gate	40
B.1	Comparison of effective and exact description	60

List of Tables

Citations to Previously Published Work

Most of the chapters of this thesis have appeared in print elsewhere. By chapter number, they are:

- Chapter 2: “Single-photon nonlinearities in two-mode optomechanics,” P. Kómár, S. D. Bennett, K. Stannigel, S. J. M. Habraken, P. Rabl, P. Zoller, and M. D. Lukin, *Phys. Rev. A* **87**, 013839 (2013).
- Chapter 3: “Optomechanical quantum information processing,” K. Stannigel, P. Kómár, S. J. M. Habraken, S. D. Bennett, M. D. Lukin, P. Zoller, and P. Rabl, *Phys. Rev. Lett.* **109**, 013603 (2012).
- Chapter 4: “Heralded Quantum Gates with Integrated Error Detection in Optical Cavities,” J. Borregaard, P. Kómár, E. M. Kessler, A. S. Sørensen, and M. D. Lukin, *Phys. Rev. Lett.* **114**, 110502 (2015).
- Chapter 5: “Long-distance entanglement distribution using individual atoms in optical cavities,” J. Borregaard, P. Kómár, E. M. Kessler, A. S. Sørensen, and M. D. Lukin, *Phys. Rev. A* **92**, 012307 (2015).
- Chapter 6: “Heisenberg-Limited Atom Clocks Based on Entangled Qubits,” E. M. Kessler, P. Kómár, M. Bishof, L. Jiang, A. S. Sørensen, J. Ye, and M. D. Lukin, *Phys. Rev. Lett.* **112**, 190403 (2014).
- Chapter 7: “A quantum network of clocks,” P. Kómár, E. M. Kessler, M. Bishof, L. Jiang, A. S. Sørensen, J. Ye, and M. D. Lukin, *Nature Physics* **10**, 582587 (2014).
- Chapter 8: “Quantum network of neutral atom clocks,” P. Kómár, T. Topcu, E. M. Kessler, A. Derevianko, A. S. Sørensen, and M. D. Lukin, *?? ??, ??* (2015?).

Acknowledgments

*Dedicated to my parents Erzsébet and Antal,
my sister Anna,
and my fiancée Szilvia.*

Chapter 1

Introduction and Motivation

1.1 Overview and Structure

1.2 Optomechanical Systems

1.3 Atom-Cavity Systems

1.4 Rydberg Interactions

1.5 Quantum Repeaters

1.6 Atomic Clocks and Quantum Metrology

Chapter 2

Single-photon nonlinearities in two-mode optomechanics

2.1 Introduction

Optomechanical systems (OMSs) involve the interaction between optical and mechanical modes arising from radiation pressure force, canonically in an optical cavity with a movable mirror [32, 41, 3, 25, 22]. Recent progress in optomechanical (OM) cooling techniques has been rapid [43, 26, 2, 33, 16, 56, 66, 69], and experiments have now demonstrated cooling to the mechanical ground state [47, 65, 11], OM induced transparency [68, 54], and coherent photon-phonon conversion [23, 67, 30]. These developments have attracted significant interest, and motivated proposals for applications exploiting OM interactions at the quantum level, ranging from quantum transducers [61, 55, 51, 63] and mechanical storage of light [72, 1, 13] to single-photon sources [49] and OM quantum information processing [60, 57]. Significant advantages

of OM platforms for these applications are the possibility for mass production and on-chip integration using nanofabrication technologies, wide tuneability and the versatility of mechanical oscillators to couple to a wide variety of quantum systems [58].

The force exerted by a single photon on a macroscopic object is typically weak; consequently, experiments have so far focused on the regime of strong optical driving, where the OM interaction is strongly enhanced but effectively linear [27, 64]. However, recent progress in the design of nanoscale OMSs [11, 21, 10, 18] and OM experiments in cold atomic systems [29, 8] suggests that the regime of single-photon strong coupling, where the OM coupling strength g exceeds the optical cavity decay rate κ , is within reach of the next generation of OM experiments. In this regime, the inherently nonlinear OM interaction is significant at the level of single photons and phonons [42, 37, 49, 46]. For example, the presence of a single photon can—via the mechanical mode—strongly influence or even block the transmission of a second photon, leading to photon blockade. This single-photon nonlinearity was recently analyzed for canonical OMSs consisting of a single optical mode coupled to a mechanical mode [49, 35, 36]. However, with a single optical mode, the OM coupling is highly off-resonant, leading to a suppression of effective photon-photon interactions by the large mechanical frequency $\omega_m \gg g$ [49].

In this paper we develop a quantum theory of a weakly driven *two-mode* OMS [44, 60, 38, 4] in which two optical modes are coupled to a mechanical mode. The key advantage of this approach is that photons in the two optical modes can be resonantly exchanged by absorbing or emitting a phonon via three-mode mixing. We extend our earlier results [60], where we discussed possible applications of resonant

optomechanics such as single-photon sources and quantum gates, by exploring one-time and two-time photon correlations of both optical modes. Specifically, we find that the photon-photon correlation function of the undriven optical mode exhibits delayed bunching for long delay times, arising from a heralded single mechanical excitation after detection of a photon in the undriven mode. Finally, we compare the two-mode OMS to the canonical atomic cavity QED system with a similar low-energy level spectrum [9, 7]. Despite several similarities we find that, in stark contrast to the atom-cavity system, the OMS studied here does *not* exhibit nonclassical correlations unless the strict strong coupling condition $g > \kappa$ is met. Our results serve as a guideline for OM experiments nearing the regime of single-photon nonlinearity, and for potential quantum information processing applications with photons and phonons.

The remainder of the paper is organized as follows. In Sec. 2.2, we introduce the system and details of the model. In Sec. 2.3, we calculate the equal-time intensity correlation functions of both transmitted and reflected photons, and discuss signatures of nonclassical photon statistics. In Sec. 2.4, we investigate two-time correlation functions of the transmitted photons, and discuss delayed coincidence correlations that indicate the heralded preparation of a single phonon state. Finally, we provide a brief outlook on the feasibility of strong OM coupling in Sec. 2.5, and conclude in Sec. 2.6 with a summary of our results. Appendix A.2 contains details of our analytic model used to derive several results discussed in the paper.

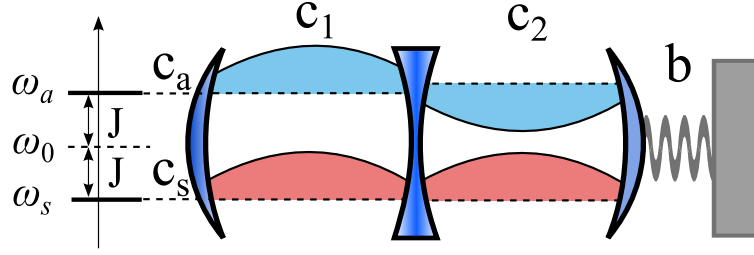


Figure 2.1: Optomechanical system consisting of two tunnel-coupled optical cavity modes c_1 and c_2 , and a mechanical oscillator b coupled to one of the cavity modes by radiation pressure. The coupled optical modes are diagonalized in terms of symmetric and antisymmetric modes, c_s and c_a .

2.2 Multimode optomechanics

We consider the setup shown schematically in Fig. 2.1, consisting of two optical cavities separated by a semitransparent mirror. The cavity modes are coupled by photons tunneling through the fixed mirror in the middle, and the mode on the right couples to the motion of a vibrating endmirror oscillator through radiation pressure. The Hamiltonian describing the system is ($\hbar = 1$)

$$\begin{aligned}
 H_0 = & \omega_0(c_1^\dagger c_1 + c_2^\dagger c_2) - J(c_1^\dagger c_2 + c_1 c_2^\dagger) \\
 & + \omega_m b^\dagger b - g(b^\dagger + b)c_2^\dagger c_2 + H_{\text{dr}}(t),
 \end{aligned} \tag{2.1}$$

where $c_{1,2}$ are annihilation operators for the two cavity modes, which we assume to be degenerate with frequency ω_0 , and J is the photon tunneling amplitude through the central mirror. The motion of the endmirror on the right is described by a single mechanical mode with annihilation operator b and frequency ω_m , and the parametric coupling strength g corresponds to the shift of the cavity frequency due to a single mechanical phonon. Finally, $H_{\text{dr}}(t) = \sum_{i=1,2} (\Omega_i c_i e^{i\omega_L t} + \text{h.c.})$ describes two coherent driving fields of amplitudes Ω_i and frequency ω_L , which are applied to the left and right cavities.

We are interested in a three-mode resonant interaction in which the two optical modes exchange a photon by absorbing or emitting a phonon in the mechanical mode. We begin by diagonalizing the optical part of H_0 in the first line of Eq. 2.1 in terms of the symmetric and antisymmetric combinations of the optical modes, $c_s = \frac{1}{\sqrt{2}}(c_1 + c_2)$ and $c_a = \frac{1}{\sqrt{2}}(c_1 - c_2)$, with eigenfrequencies $\omega_{a,s} = \omega_0 \pm J$. In the frame rotating at the laser frequency ω_L we obtain

$$\begin{aligned} H' = & -\Delta c_a^\dagger c_a - (\Delta + 2J)c_s^\dagger c_s + \omega_m b^\dagger b \\ & + \frac{g}{2} (c_a^\dagger c_s + c_s^\dagger c_a) (b + b^\dagger) + \sum_{\eta=s,a} \Omega_\eta (c_\eta^\dagger + c_\eta), \end{aligned} \quad (2.2)$$

where $\Delta = \omega_L - \omega_a$ is the laser detuning from the c_a mode, and $\Omega_{s,a} = (\Omega_1 \pm \Omega_2)/\sqrt{2}$. Next, we focus on the case of three-mode resonance, $\omega_m = 2J$, and assume $\omega_m \gg g, |\Delta|, \Omega_i$. The third inequality here corresponds to a weak optical drive, the relevant limit for studying single-photon nonlinear effects in this work. This allows us to make a rotating wave approximation with respect to the remaining large frequency scale ω_m , and in the frame defined by the transformation $U = \exp[-i\omega_m t(b^\dagger b - c_s^\dagger c_s)]$, the Hamiltonian H' simplifies to

$$H = -\Delta(c_a^\dagger c_a + c_s^\dagger c_s) + \frac{g}{2}(c_a^\dagger c_s b + b^\dagger c_s^\dagger c_a) + \Omega_a(c_a^\dagger + c_a). \quad (2.3)$$

This is the starting point for our analysis discussed below. Note that the assumptions made in deriving Eq. (2.3) are fulfilled in most experimental systems of interest [28, 73], and H represents a generic description for resonant two-mode optomechanics [44, 19, 15, 38].

The nonlinear terms proportional to g in Eq. (2.3) describe coherent photon exchange between the two optical modes mediated by absorption or emission of a

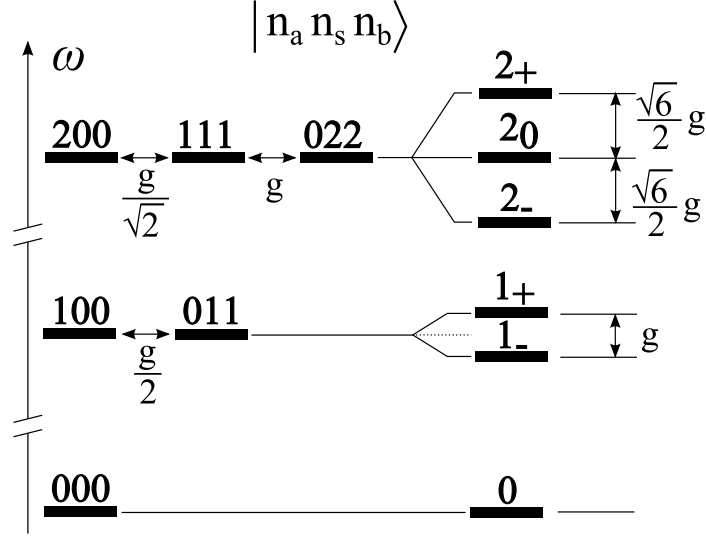


Figure 2.2: Level diagram showing the relevant zero-, one- and two-photon states at zero temperature and under the three-mode resonance condition $\omega_s - \omega_a = \omega_m$. States are labeled by $|n_a n_s n_b\rangle$ denoting the number n_a (n_s) of antisymmetric (symmetric) photons and the number of phonons n_b . The optomechanical coupling g splits the degeneracy of states $|n_a n_s n_b\rangle$ and $|n_a - 1, n_s + 1, n_b + 1\rangle$.

phonon. The resulting low energy level diagram is shown in Fig. 2.2, where $|n_a n_s n_b\rangle$ represents a state with n_a and n_s photons in the c_a and c_s modes, and n_b phonons in the mechanical mode. In the absence of a drive we diagonalize H in this few-photon subspace, yielding the eigenstates

$$|0\rangle = |000\rangle, \quad (2.4)$$

$$|1_{\pm}\rangle = \frac{1}{\sqrt{2}} (|100\rangle \pm |011\rangle), \quad (2.5)$$

$$|2_{\pm}\rangle = \frac{1}{\sqrt{6}} (|200\rangle \pm \sqrt{3}|111\rangle + \sqrt{2}|022\rangle), \quad (2.6)$$

$$|2_0\rangle = \frac{1}{\sqrt{3}} (\sqrt{2}|200\rangle - |022\rangle). \quad (2.7)$$

Note that in the diagonal basis the weak driving field couples all states with photon number differing by one. In the following sections we use this low energy Hilbert space to understand photon correlations in the system.

In addition to the coherent evolution modeled by the Hamiltonian H , we describe optical and mechanical dissipation using a master equation for the system density operator ρ ,

$$\dot{\rho} = -i[H, \rho] + \kappa \mathcal{D}[c_a]\rho + \kappa \mathcal{D}[c_s]\rho \quad (2.8)$$

$$+ \frac{\gamma}{2}(N_{\text{th}} + 1)\mathcal{D}[b]\rho + \frac{\gamma}{2}N_{\text{th}}\mathcal{D}[b^\dagger]\rho, \quad (2.9)$$

where H is given by Eq. 2.3, 2κ and γ are energy decay rates for the optical and mechanical modes, respectively, N_{th} is the thermal phonon population and $\mathcal{D}[\hat{o}]\rho = 2\hat{o}\rho\hat{o}^\dagger - \hat{o}^\dagger\hat{o}\rho - \rho\hat{o}^\dagger\hat{o}$. Below we study nonlinear effects at the level of single photons, both numerically and analytically, by solving Eq. 2.8 approximately in the limit of weak optical driving, $\Omega \equiv \Omega_a \ll \kappa$.

2.3 Equal-time correlations

2.3.1 Average transmission and reflection

Before focussing on photon-photon correlations, we first study the average transmission through the cavity, which is proportional to the mean intracavity photon number. In Fig. 2.3 and 2.4 we show the intracavity photon number of the two optical modes,

$$\bar{n}_i = \left\langle c_i^\dagger c_i \right\rangle, \quad (2.10)$$

where $i = a, s$, and angle brackets denote the steady state average. At $\Delta/g = \pm\frac{1}{2}$, both transmission curves exhibit a maximum, indicating that the driving field is in resonance with an eigenmode of the system. The position of these peaks can

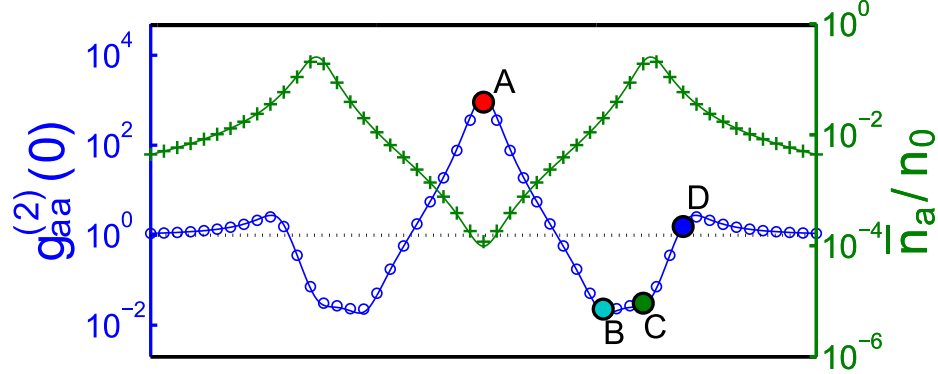


Figure 2.3: Normalized average photon number (green “+”) and photon-photon correlation function (blue “o”) for driven mode c_a as a function of laser detuning at zero temperature. Solid lines are calculated from analytic model (see Eqs. (2.19-2.24)) and points show full numerical calculation. The average photon number is normalized by $n_0 = (\Omega/\kappa)^2$. ($g/\kappa = 20$ and $\gamma/\kappa = 0.2$)

be understood from the level diagram shown in Fig. 2.2, which at finite g shows a splitting of the lowest photonic states into a doublet, $|1_{\pm}\rangle = (|100\rangle \pm |011\rangle)/\sqrt{2}$.

In addition to the transmission, we plot the mean reflected photon number in Fig. 2.5. As discussed below, the reflected photon statistics can also exhibit signatures of nonlinearity. We calculate properties of the reflected light using the annihilation operator $c_R = c_a + i\frac{\Omega}{\kappa}$, obtained from standard input-output relations for a symmetric two-sided cavity (see Appendix A.1). The mean reflected photon number $\bar{n}_R = \langle c_R^\dagger c_R \rangle$ is plotted in Fig. 2.5. At $\Delta/g = \pm\frac{1}{2}$, the average reflection has a minimum where the average transmission has a maximum. Note that in contrast to a single cavity, even on resonance the transmission probability is less than unity and the reflection probability remains finite.

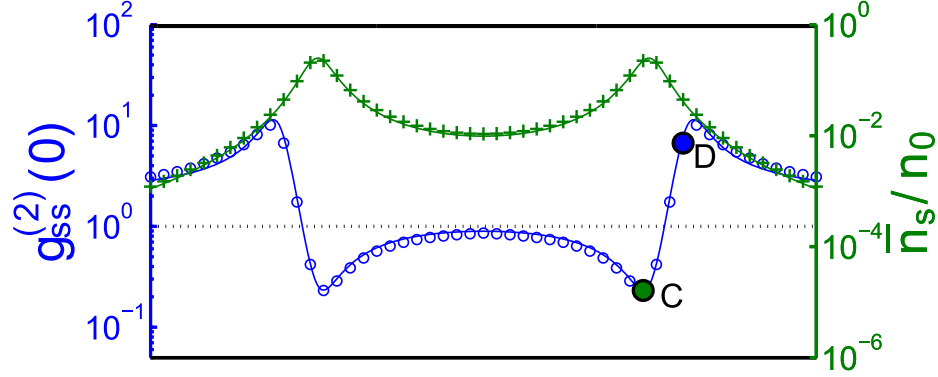


Figure 2.4: Normalized average photon number (green “+”) and photon-photon correlation function (blue “o”) for the undriven mode c_s as a function of laser detuning at zero temperature. Solid lines are calculated from analytic model (see Eqs. (2.19-2.24)) and points show full numerical calculation. The average photon number is normalized by $n_0 = (\Omega/\kappa)^2$. ($g/\kappa = 20$ and $\gamma/\kappa = 0.2$)

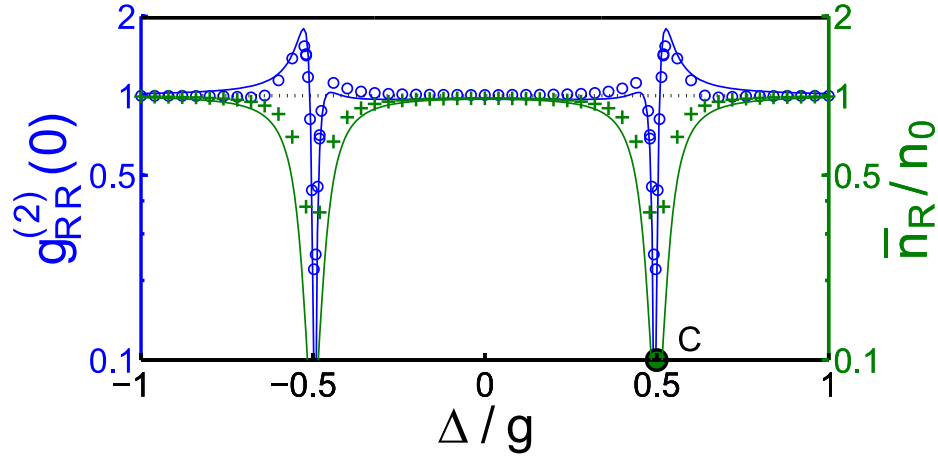


Figure 2.5: Normalized average photon number (green “+”) and photon-photon correlation function (blue “o”) for the reflected field c_R , as a function of laser detuning at zero temperature. Solid lines are calculated from analytic model (see Eqs. (2.19-2.24)) and points show full numerical calculation. The average photon number is normalized by $n_0 = (\Omega/\kappa)^2$. The small discrepancy between the analytic and numerical results is due to the approximation $g/\kappa \gg 1$ to simplify the expressions in Eqs. (2.19-2.24) ($g/\kappa = 20$ and $\gamma/\kappa = 0.2$)

2.3.2 Intensity correlations

To characterize nonclassical photon statistics in the light transmitted through the OMS we study the equal-time photon-photon correlation functions,

$$g_{ii}^{(2)}(0) = \frac{\langle c_i^\dagger c_i^\dagger c_i c_i \rangle}{\langle c_i^\dagger c_i \rangle^2}, \quad (2.11)$$

where all operators are evaluated at the same time and $i = a, s, R$. A normalized correlation of $g_{ii}^{(2)}(0) < 1$ indicates photon anti-bunching, and the limit $g_{ii}^{(2)}(0) \rightarrow 0$ corresponds to the complete photon blockade regime in which two photons never occupy the cavity at the same time. The solid curves show $g_{aa}^{(2)}(0)$ in Fig. 2.3, $g_{ss}^{(2)}(0)$ in Fig. 2.4 and $g_{RR}^{(2)}(0)$ in Fig. 2.5 as a function of the laser detuning and in the limit of weak driving $\Omega/\kappa \ll 1$. The most pronounced features of these correlation functions occur at $|\Delta|/g = 0, \frac{1}{\sqrt{8}}, \frac{1}{2}$ and $\frac{\sqrt{6}}{4}$, as marked by dots A, B, C and D, respectively. As we explain in detail in the following analysis, we find that the photon bunching at A and anti-bunching at B are the result of destructive quantum interference, while the features at points C and D arise from one- and two-photon resonances.

To gain insight into the two photon correlation functions shown in Fig. 2.3, 2.4 and 2.5, we develop an approximate analytic model for the system by considering only the six levels shown in Fig. 2.2. Assuming that the system is initially prepared in $|000\rangle$, these are the only levels significantly populated by weakly driving the c_a mode. We make the ansatz [9]

$$\begin{aligned} |\psi\rangle = & A_{000}|000\rangle + A_{100}|100\rangle + A_{011}|011\rangle \\ & + A_{200}|200\rangle + A_{111}|111\rangle + A_{022}|022\rangle, \end{aligned} \quad (2.12)$$

and describe the dynamics by evolving $|\psi\rangle$ under the action of the non-Hermitian

Hamiltonian, $\tilde{H} = H - i [\kappa c_a^\dagger c_a + \kappa c_s^\dagger c_s + \frac{\gamma}{2} b^\dagger b]$. This approach allows us to evaluate intensities up to order Ω^2 and two-point correlation up to order Ω^4 , since the neglected quantum jumps lead to higher order corrections. By neglecting the typically small mechanical decay rate $\gamma \ll \kappa$, the amplitudes in Eq. 2.12 then satisfy

$$\dot{A}_{000} = 0, \quad (2.13)$$

$$\dot{A}_{100} = -i\frac{g}{2}A_{011} - i\Omega A_{000} - \tilde{\kappa}A_{100}, \quad (2.14)$$

$$\dot{A}_{011} = -i\frac{g}{2}A_{100} - \tilde{\kappa}A_{011}, \quad (2.15)$$

$$\dot{A}_{200} = -i\frac{g}{\sqrt{2}}A_{111} - i\sqrt{2}\Omega A_{100} - 2\tilde{\kappa}A_{200}, \quad (2.16)$$

$$\dot{A}_{111} = -i\frac{g}{\sqrt{2}}A_{200} - igA_{022} - i\Omega A_{011} - 2\tilde{\kappa}A_{111}, \quad (2.17)$$

$$\dot{A}_{022} = -igA_{111} - 2\tilde{\kappa}A_{022}, \quad (2.18)$$

where $\tilde{\kappa} = \kappa - i\Delta$. It is straightforward to solve Eqs. (2.13–2.18) for the steady state amplitudes (see Appendix A.2). To lowest order in Ω/κ the mean occupation numbers are $\bar{n}_a = |\bar{A}_{100}|^2$, $\bar{n}_s = |\bar{A}_{011}|^2$ and $\bar{n}_R = |\bar{A}_{100} + i\Omega/\kappa|^2$, where \bar{A} denote steady state amplitudes. We obtain

$$\frac{\bar{n}_a}{n_0} = \frac{\kappa^2 [R_\kappa(0)]^{1/2}}{R_\kappa\left(\frac{g}{2}\right)}, \quad (2.19)$$

$$\frac{\bar{n}_s}{n_0} = \frac{g^2 \kappa^2}{4R_\kappa\left(\frac{g}{2}\right)}, \quad (2.20)$$

$$\frac{\bar{n}_R}{n_0} \approx \frac{[R_{\kappa/2}\left(\frac{g}{2}\right)]^2}{[R_\kappa\left(\frac{g}{2}\right)]^2}, \quad (2.21)$$

where $R_K(\omega) = [K^2 + (\Delta - \omega)^2][K^2 + (\Delta + \omega)^2]$ and $n_0 = (\Omega/\kappa)^2$. From the factors $R_K(\omega)$ in the denominators (numerators) in these expressions, we obtain the positions of the resonances (antiresonances) in the average intracavity photon numbers, in

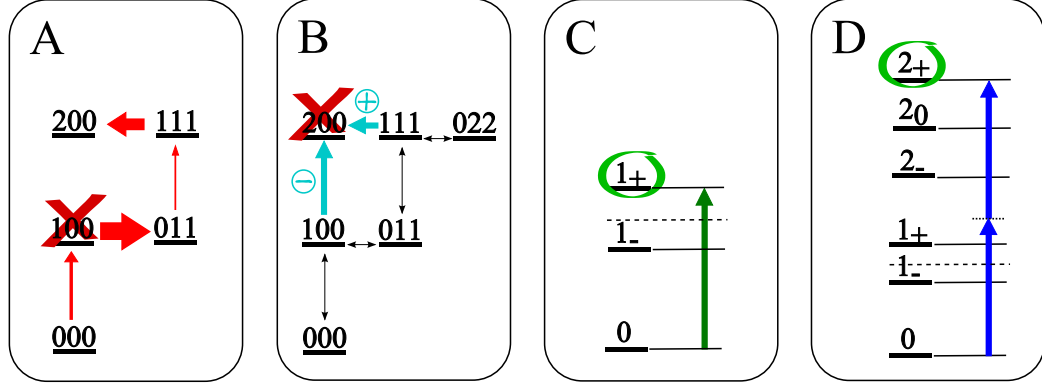


Figure 2.6: Illustration of the origin of the features marked with A,B,C and D on Fig. 2.3, 2.4 and 2.5 as explained in the text. Suppression (enhancement) of the steady state population of a specific level is indicated by a red X (green circle).

excellent agreement with the numerical results shown in Fig. 2.3, 2.4 and 2.5. Our six-level model also provides the equal-time correlations (see Appendix A.2),

$$g_{aa}^{(2)}(0) = \frac{R_{\kappa}\left(\frac{g}{\sqrt{8}}\right) R_{\kappa}\left(\frac{g}{2}\right)}{R_{\kappa}(0) R_{\kappa}\left(\frac{\sqrt{6}}{4}g\right)}, \quad (2.22)$$

$$g_{ss}^{(2)}(0) = \frac{2R_{\kappa}\left(\frac{g}{2}\right)}{R_{\kappa}\left(\frac{\sqrt{6}}{4}g\right)}, \quad (2.23)$$

$$g_{RR}^{(2)}(0) \approx \frac{R_{\kappa}\left(\frac{g}{2}\right) R_{16\kappa^3/g^2}\left(\frac{g}{2} - \frac{2\kappa^2}{g}\right)}{\left[R_{\kappa/2}\left(\frac{g}{2}\right)\right]^2}. \quad (2.24)$$

Again, these expressions are in agreement with the features seen in the numerical results in Fig. 2.3, 2.4 and 2.5. The positions of maxima and minima are seen directly by the arguments of the factors $R_K(\omega)$. Note that we assumed $g/\kappa \gg 1$ to obtain the simplified expressions in Eqs. (2.22-2.24), but we retained the shift of order $g(\kappa/g)^2$ in the argument in Eq. 2.24 because this shift is larger than the width of the antiresonance.

We now discuss each feature in Fig. 2.3, 2.4 and 2.5 in terms of our six-level model together with the diagonal basis in Eqs. (2.4-2.7). First, at detuning $\Delta = 0$ (point

A in Fig. 2.3) we see $g_{aa}^{(2)}(0) > 1$, indicating bunching. This is due to destructive interference that suppresses the population in $|100\rangle$ (panel A in Fig. 2.6), and can be understood as the system being driven into a dark state, $|d\rangle \propto g|000\rangle - \Omega|011\rangle$, similar to electromagnetically induced transparency (EIT) [39, 68]. In the dark state, $|011\rangle$ remains populated, allowing transitions to $|111\rangle$ which in turn is strongly coupled to $|200\rangle$. The net result is a relative suppression of the probability to have one photon compared to two photons in the driven mode, leading to bunching at $\Delta = 0$. Second, at detuning $\Delta = g/\sqrt{8}$ (point B), mode c_a shows anti-bunching due to a suppressed two-photon probability. Again, this is due to destructive interference, or the presence of a dark state in which $|200\rangle$ remains unpopulated (panel B). Third, at detuning $\Delta = \frac{g}{2}$ (point C), all modes show anti-bunching. This is due to a one-photon resonant transition $|0\rangle \rightarrow |1_+\rangle$ (panel C). Finally, at detuning $\Delta = \frac{\sqrt{6}}{4}g$ (point D), both c_a and c_s show bunching due to a two-photon resonant transition $|0\rangle \rightarrow |2_+\rangle$ (panel D).

2.3.3 Absence of two-photon resonance at $\Delta = 0$

At first glance, the level diagram in Fig. 2.2 together with bunching in Fig. 2.3 suggest a two-photon resonance at zero detuning $\Delta = 0$, where the energy of the eigenstate $|2_0\rangle$ is equal to the energy of two drive photons. However, as discussed above, the bunching at $\Delta = 0$ arises entirely from the suppression of a one-photon population; further, we find that the expected two-photon resonance is cancelled by interference. This can be seen from a second order perturbative calculation of the two-photon Rabi frequency $\Omega_{0,2_0}^{(2)}$ for the transition $|0\rangle \rightarrow |2_0\rangle$. The two-photon state

$|2_0\rangle$ can be populated by the drive $H_{\text{dr}} = \Omega(c_a^\dagger + c_a)$ from state $|0\rangle$ via two intermediate one-photon eigenstates, $|1_\pm\rangle$ given by Eq. 2.5, with energies $\omega_{1\pm} = -\Delta \pm \frac{g}{2}$ in the rotating frame. The resulting Rabi frequency is

$$\Omega_{0,2_0}^{(2)} = \sum_{n=1_-,1_+} \frac{\langle 2_0 | H_{\text{dr}} | n \rangle \langle n | H_{\text{dr}} | 0 \rangle}{\omega_n}, \quad (2.25)$$

which vanishes at $\Delta = 0$ as a consequence of destructive interference between the two amplitudes. The exact cancellation is lifted by including finite dissipation and the full spectrum; nonetheless this simple argument shows that the expected two-photon resonance at $\Delta = 0$ is strongly suppressed.

Further evidence of the absence of a two-photon resonance at $\Delta = 0$ is the lack of bunching in the undriven mode in Fig. 2.4. If there were a two-photon resonance, one would expect that bunching should also occur in the undriven mode, since the state $|2_0\rangle$ involves both c_a and c_s modes. This is indeed the case at detuning $\Delta = \frac{\sqrt{6}}{4}g$ (see point D in Fig. 2.4), where both modes show bunching as a result of two-photon resonance. In contrast, we see no bunching in the undriven mode at $\Delta = 0$. This supports our conclusion that the observed bunching at $\Delta = 0$ arises from suppression of population in $|100\rangle$ due to interference, as discussed in Section 2.3.2, and not from two-photon resonance. As discussed above, this interference does not suppress population in $|011\rangle$, so we do not expect bunching in the c_s mode from this effect.

Finally, to confirm our intuitive picture we plot the intensity correlation function, $g_{\text{tot}}^{(2)}(0) = \langle n_{\text{tot}}(n_{\text{tot}} - 1) \rangle / \langle n_{\text{tot}} \rangle^2$, of the total photon number, $n_{\text{tot}} = n_a + n_s$, in the coupled OM system in Fig. 2.7. The probability to find one photon in the combined cavity is maximal at $\Delta/g = \pm \frac{1}{2}$ due to one-photon resonance. Similarly, we observe antibunching at point C and bunching at point D, due to interference and two-photon

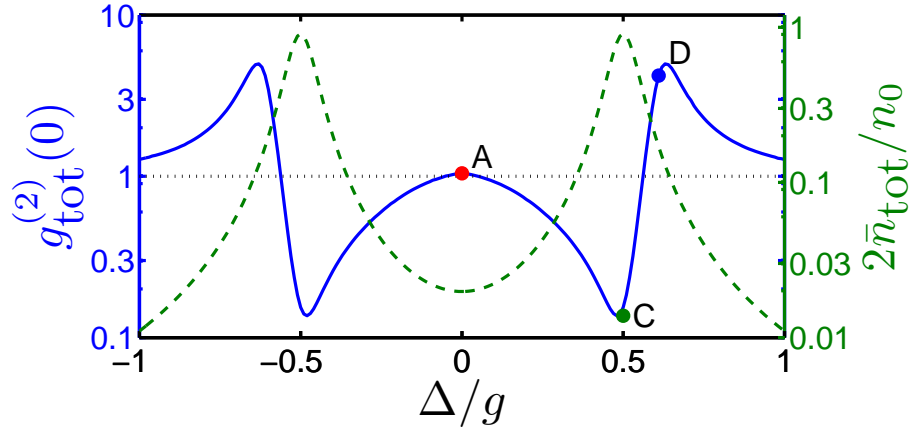


Figure 2.7: Average number (green dashed) and intensity correlation (blue solid) of total photon number in the coupled OM system. Parameters are the same as in Fig. 2.3, and dots mark the same detunings. One- and two-photon resonances are seen at C and D, but we see no bunching in the total photon number at $\Delta = 0$ (point A). This reflects the lack of two-photon resonance due to destructive interference (see Eq. 2.25).

resonance respectively, as discussed in Section 2.3.2. However, we find neither bunching nor antibunching at $\Delta = 0$, demonstrating the absence of a two-photon resonance despite the fact that $|2_0\rangle$ lies at twice the drive frequency.

2.3.4 Finite temperature

So far in our analysis we have focused on the case where the mechanical system is prepared in its vibrational ground state, $|0_m\rangle$. This condition can be achieved using high frequency resonators operated at cryogenic temperatures [47], and in the limit of weak driving $\Omega/\kappa \ll 1$ such that optical heating of the mechanical mode can be neglected. The mechanical groundstate could also be prepared using OM cooling [43, 26, 2, 33, 16, 56, 66, 69, 47, 65, 11], using an optical mode far-detuned from the ones we consider here for nonlinear interactions [60]. Nonetheless, in the following we

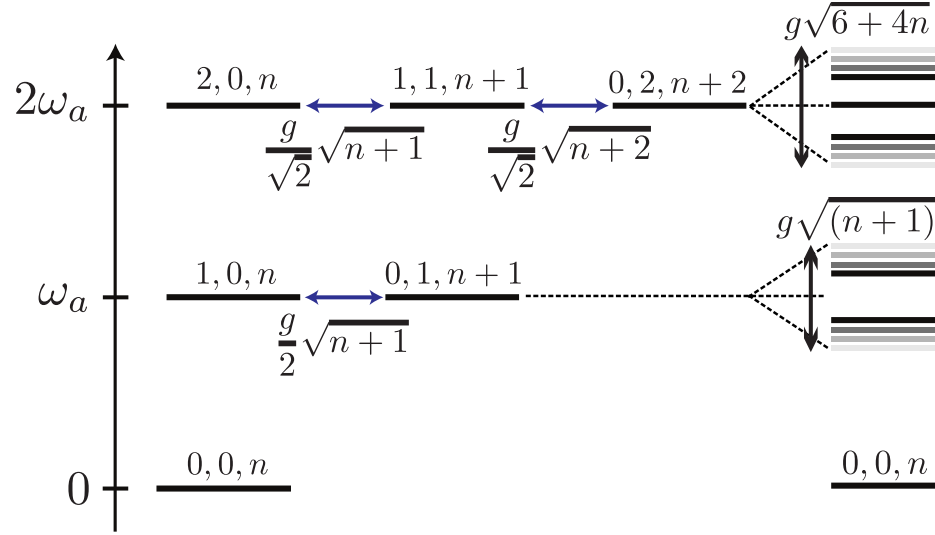


Figure 2.8: Level diagram showing the six states populated by the drive from level $|0, 0, n\rangle$ (left), and the associated eigenmodes (right) with n -dependent splittings.

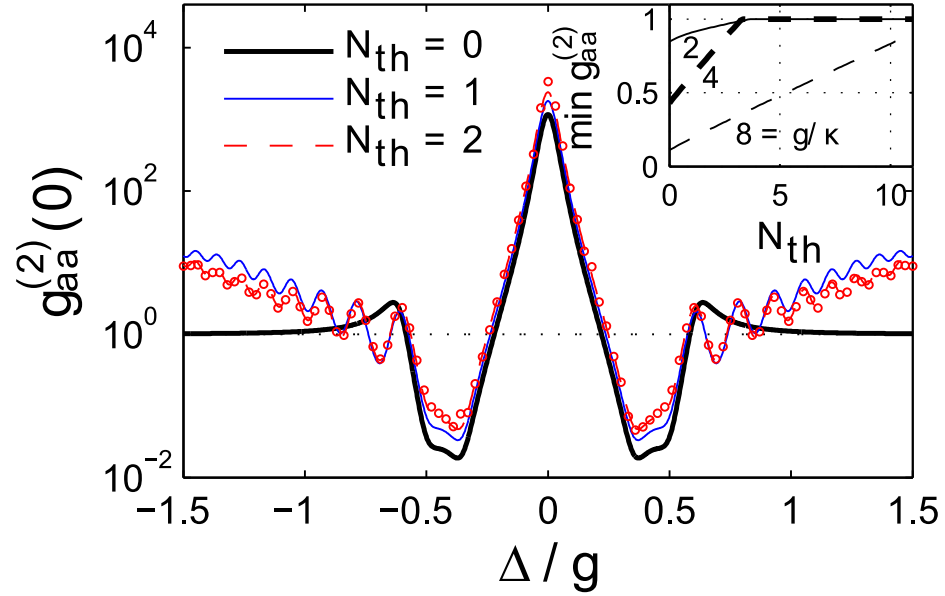


Figure 2.9: Driven mode correlation function $g_{aa}^{(2)}(0)$ for thermal mechanical occupation $N_{th} = 0, 1, 2$. Solid lines show the analytic calculation with $\gamma \rightarrow 0$, and dots show the full numerical results for $N_{th} = 2$ only. The inset shows the minimal $g_{aa}^{(2)}(0)$ as a function of N_{th} for several coupling strengths. Parameters are $g/\kappa = 20$, and (for numerics) $\gamma/\kappa = 10^{-3}$.

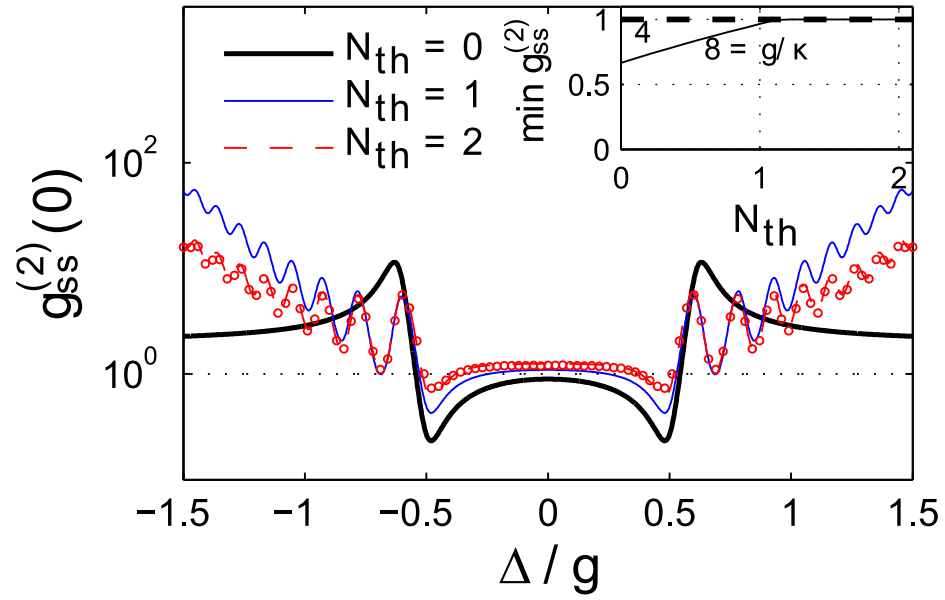


Figure 2.10: Undriven mode correlation function $g_{ss}^{(2)}(0)$ for thermal mechanical occupation $N_{\text{th}} = 0, 1, 2$. Solid lines show the analytic calculation with $\gamma \rightarrow 0$, and dots show the full numerical results for $N_{\text{th}} = 2$ only. The inset shows the minimal $g_{ss}^{(2)}(0)$ as a function of N_{th} for several coupling strengths. Parameters are $g/\kappa = 20$, and (for numerics) $\gamma/\kappa = 10^{-3}$.

extend our analytic treatment to the case of finite temperature, and show that many of the nonclassical features are robust even in the presence of small but finite thermal occupation of the mechanical mode.

To generalize our previous results we now consider a finite equilibrium occupation number $N_{\text{th}} > 0$ of the mechanical mode, but still assume that $\gamma(N_{\text{th}} + 1) \ll \kappa, g$. Within this approximation we proceed as above, and make a similar six-level ansatz as in Eq. (2.12) for each phonon number n ,

$$\begin{aligned} |\psi_n\rangle = & A_{0,0,n}|0, 0, n\rangle + A_{1,0,n}|1, 0, n\rangle \\ & + A_{0,1,n+1}|0, 1, n+1\rangle + A_{2,0,n}|2, 0, n\rangle \\ & + A_{1,1,n+1}|1, 1, n+1\rangle + A_{0,2,n+2}|0, 2, n+2\rangle, \end{aligned} \quad (2.26)$$

where $|\psi_n\rangle$ includes states up to two photons that are connected by the weak drive and coupling g , starting from the state $|00n\rangle$. As shown in Fig. 2.8 the coupling between the states within each six-level subspace depends explicitly on the phonon number n . Following the same approach as above, the amplitudes in Eq. (2.26) evolve according to

$$\dot{A}_{0,0,n} = 0, \quad (2.27)$$

$$\dot{A}_{1,0,n} = -i\frac{g}{2}\sqrt{n+1}A_{0,1,n+1} - i\Omega A_{0,0,n} - \tilde{\kappa}A_{1,0,n}, \quad (2.28)$$

$$\dot{A}_{0,1,n+1} = -i\frac{g}{2}\sqrt{n+1}A_{1,0,n} - \tilde{\kappa}A_{0,1,n+1}, \quad (2.29)$$

$$\dot{A}_{2,0,0} = -ig\sqrt{\frac{n+1}{2}}A_{1,1,n+1} - i\sqrt{2}\Omega A_{1,0,n} - 2\tilde{\kappa}A_{2,0,n}, \quad (2.30)$$

$$\dot{A}_{1,1,n+1} = -ig\sqrt{\frac{n+1}{2}}A_{2,0,n} - ig\sqrt{\frac{n+2}{2}}A_{0,2,n+2} - i\Omega A_{0,1,n+1} - 2\tilde{\kappa}A_{1,1,n+1}, \quad (2.31)$$

$$\dot{A}_{0,2,n+2} = -ig\sqrt{\frac{n+2}{2}}A_{1,1,n+1} - 2\tilde{\kappa}A_{0,2,n+2}. \quad (2.32)$$

We solve for the steady state amplitudes within each subspace n and average the result over the initial thermal phonon distribution, assuming no coupling between subspaces due to the small phonon relaxation rate. We obtain the average photon numbers

$$\bar{n}_a = \sum_n \zeta_n |\bar{A}_{1,0,n}|^2, \quad \bar{n}_s = \sum_n \zeta_n |\bar{A}_{0,1,n+1}|^2, \quad (2.33)$$

where $\zeta_n = e^{-\beta\hbar\omega_m n}(1 - e^{-\beta\hbar\omega_m})$ and $\beta^{-1} = k_B T$. Similarly, the $g_{ii}^{(2)}(0)$ functions are given by

$$g_{aa}^{(2)}(0) = 2 \sum_n \zeta_n |\bar{A}_{2,0,n}|^2 / \bar{n}_a^2, \quad (2.34)$$

$$g_{ss}^{(2)}(0) = 2 \sum_n \zeta_n |\bar{A}_{0,2,n+2}|^2 / \bar{n}_s^2. \quad (2.35)$$

We provide the expressions for the steady state amplitudes $\bar{A}_{2,0,n}$ and $\bar{A}_{0,2,n+2}$ in the Appendix A.2.

We plot the correlation functions, $g_{aa}^{(2)}(0)$ in Fig. 2.9 and $g_{ss}^{(2)}(0)$ in Fig. 2.10 for different thermal phonon numbers, N_{th} . Solid lines were calculated from the above analytic approach with $\gamma \rightarrow 0$, and we find excellent agreement with the full numerical results including small but finite γ (dots, shown only for thermal occupation $N_{\text{th}} = 2$). We see that the zero temperature features such as antibunching survive at finite temperature for sufficiently strong coupling [60]. In the insets we plot the minimum antibunching as a function of thermal occupation number for several ratios g/κ . Antibunching remains visible up to a critical thermal phonon number, set by g/κ , beyond which the contributions from different phonon numbers smear out the effect and antibunching vanishes. In addition, for detunings $|\Delta| > g/2$, a series of

new resonances appear in the correlation functions, and for small but finite occupation numbers we find new antibunching features that are absent for $N_{\text{th}} = 0$. These new features can be understood from the n -dependent splitting of the one- and two-photon manifolds as indicated in Fig. 2.8. For higher temperatures the individual resonances start to overlap, and we observe an overall increase over a broad region of large positive and negative detunings due to the cumulative effect of different phonon numbers.

2.4 Delayed coincidence and single phonon states

In addition to the equal-time correlations discussed above, quantum signatures can also be manifested in photon intensity correlations with a finite time delay. We now turn to a discussion of delayed coincidence characterized by the two-time intensity correlations functions,

$$g_{ii}^{(2)}(\tau) = \frac{\langle c_i^\dagger(0)c_i^\dagger(\tau)c_i(\tau)c_i(0) \rangle}{\langle c_i^\dagger c_i \rangle^2}, \quad (2.36)$$

for both driven and undriven modes, $i = a, s$. Expressing this correlation in terms of a classical light intensity I , $g^{(2)}(\tau) = \langle I(\tau)I(0) \rangle / \langle I \rangle^2$, and using the Schwarz inequality, we obtain the inequalities [9, 7],

$$g^{(2)}(\tau) \leq g^{(2)}(0), \quad (2.37)$$

$$|g^{(2)}(\tau) - 1| \leq |g^{(2)}(0) - 1|. \quad (2.38)$$

Similar to the classical inequality $g^{(2)}(0) > 1$ at zero delay, violation of either of these inequalities at finite delay is a signature of quantum light. We calculate the delayed

coincidence correlation functions for both the driven and undriven modes.

2.4.1 Driven mode

The correlation function $g_{aa}^{(2)}(\tau)$ is shown in Fig. 2.11(a) for two values of the detuning Δ . The most striking feature is the apparent vanishing of $g_{aa}^{(2)}(\tau)$ at several values of τ when the detuning is $\Delta = 0$ (curve A in Fig. 2.11(a)). These are due to Rabi oscillations at frequency $g/2$ following the detection of a photon. This vanishing of the finite delay correlation function is reminiscent of wavefunction collapse that occurs in a cavity containing an atomic ensemble [9], and while its origins are similar, there are important differences as we now discuss.

We can understand the finite delay intensity correlations in terms of the simple six-level model discussed in the previous section. We extend this model to describe finite delay correlations by considering the effect of photodetection on the steady state of the system. Detection of a photon in the driven mode projects the system onto the conditional state [24],

$$|\psi^a\rangle = \frac{c_a|\psi\rangle}{||c_a|\psi\rangle||}, \quad (2.39)$$

where $|\psi\rangle$ is given by Eq. 2.12 with steady state amplitudes and $||\cdot||$ denotes normalization after the jump. The conditional state $|\psi^a\rangle$ has an *increased* amplitude A_{100} after the jump (see jump at $\tau = 0$ in Fig. 2.11 (b)). Following this initial photodetection, the amplitude A_{100} subsequently undergoes Rabi oscillations with frequency $g/2$, and decays back to its steady state at rate 2κ . For sufficiently large bunching at zero delay and strong coupling $g > \kappa$, the Rabi oscillations of the amplitude $A_{100}(\tau)$ can cause it to cross zero several times before it decays back to steady state. As the

probability to detect a second photon is dominated by A_{100} , its zeros are responsible for the zeros in the correlation function $g_{aa}^{(2)}(\tau)$ zero at these delay times.

The zeros in $g^{(2)}(\tau)$ appear similar to those exhibited in a cavity strongly coupled to an atomic ensemble [9, 52, 7] or a single atom [14]. However, in stark contrast to the atomic case, the zeros in Fig. 2.11(a) are the result of Rabi oscillations following the initial quantum jump. This is qualitatively different from the atomic case, where the change in sign of the relevant amplitude (the analogy of A_{100}) occurs *immediately* after the jump itself, and the amplitude is damped back to steady state at the atomic decay rate Γ , without Rabi oscillation. As a consequence, the vanishing correlation function in the atomic case occurs at a delay set by $\tau_0 \sim \gamma^{-1} \ln C$, requiring only strong cooperativity $C = g^2/\kappa\gamma > 1$ to be visible. On the other hand, the zeros in Fig. 2.11(a) occur at delay times set by $\tau \sim 1/g$, requiring strictly strong coupling $g > \kappa$.

Before moving on to correlations of the undriven mode, we briefly discuss the correlations of the driven mode at the other value of detuning shown in Fig. 2.11(a). At detuning $\Delta = \frac{g}{\sqrt{2}}$ (curve E), which shows bunching at zero time, $g_{aa}^{(2)}(0) \gtrsim 1$, increases above its initial value at finite delay. This is a violation of the classical inequality in Eq. 2.37, and is an example of “delayed bunching,” or an increased probability to detect a second photon at a finite delay time. A similar effect was recently studied in a single mode OMS [35]. However, like the Rabi oscillations, the increased correlation function decays back to its steady state value of 1 on the timescale of κ^{-1} .

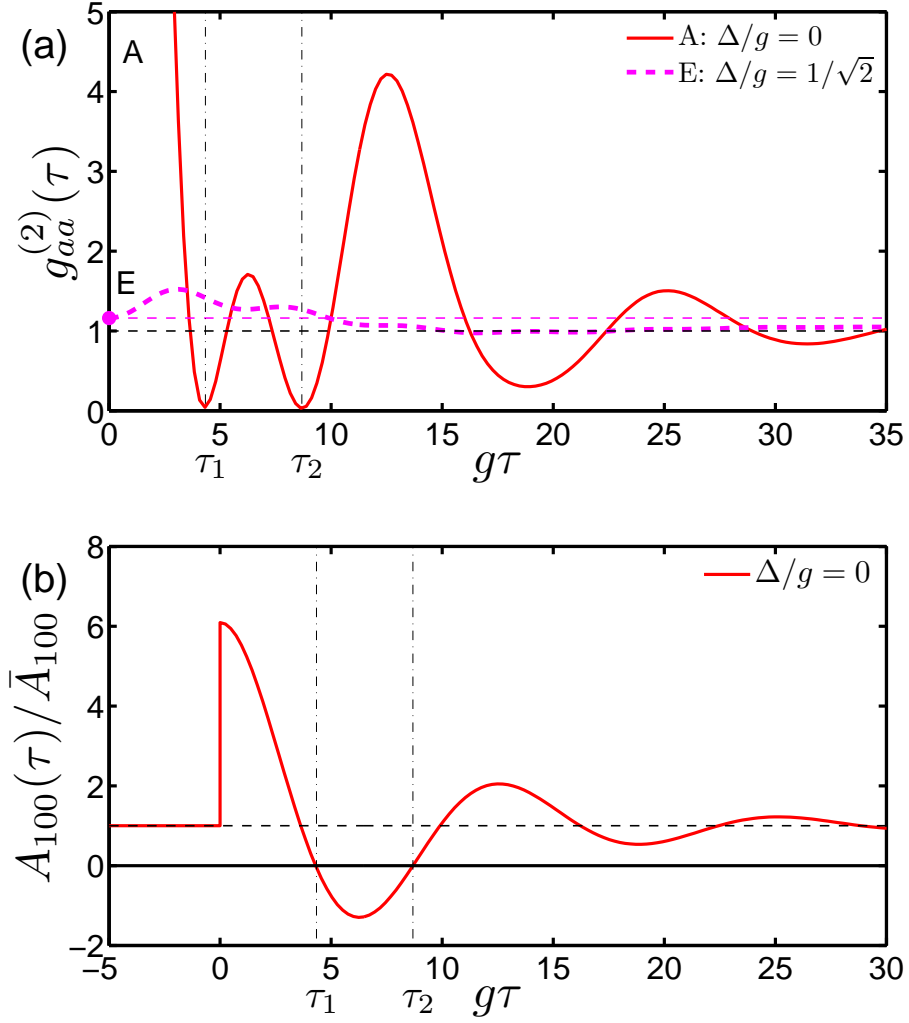


Figure 2.11: (a) Finite time delay intensity correlation function $g_{aa}^{(2)}(\tau)$ for detunings $\Delta/g = 0$ (A) and $\frac{1}{\sqrt{2}}$ (E). Detuning for curve A is the same as marked in Fig. 2.3, while E shows a new effect not seen at equal times. Thin dashed line indicates the classical bound (see Eq. 2.37) for curve E. (b) Evolution of amplitude A_{100} (normalized by its steady state value) at detuning A, $\Delta/g = 0$, after detecting a driven c_a photon at $\tau = 0$. Vertical dash-dotted lines mark delay times (τ_1, τ_2) where this amplitude vanishes resulting in the vanishing of $g_{aa}^{(2)}(\tau)$ in (a). Parameters are $g/\kappa = 8$ and $\gamma/\kappa = 0.02$.

2.4.2 Heralded single phonon states

We now turn to a discussion of the delayed coincidence correlations of the undriven mode c_s . We note that correlations of the driven and undriven modes can be measured separately provided sufficient frequency resolution, smaller than the mechanical frequency. The correlation function $g_{ss}^{(2)}(\tau)$ of the undriven mode is shown in Fig. 2.12 for several values of detuning. Similar to the driven mode, the correlation function of the undriven mode exhibits Rabi oscillations that decay on the short optical timescale $1/\kappa$. For detuning $\Delta = 0$ and $\Delta/g = \frac{\sqrt{6}}{4}$ (curves A and D in Fig. 2.12), the correlation $g_{ss}^{(2)}(\tau)$ is described by our previous six-level model of Eqs. (2.13–2.18). However, at detuning $\Delta = \frac{g}{\sqrt{2}}$ (curve E), we see that $g_{ss}^{(2)}(\tau)$ has a long tail that decays on the much longer mechanical timescale $1/\gamma$. This is due to the heralded preparation of a single phonon by detection of a photon in the undriven mode, as we now discuss.

The increase in delayed coincidence can be understood by extending the above analytic six-level model to account for the conditional state of the system after detection of a photon in the undriven mode. To do this, we simply add three additional states to the six-level ansatz in Eq. 2.12,

$$|\psi\rangle = \cdots + A_{001}|001\rangle + A_{101}|101\rangle + A_{012}|012\rangle, \quad (2.40)$$

since these are the states populated by detection of a c_s photon from the original six states (see Fig. 2.13). Using the same approach as before, we obtain the following

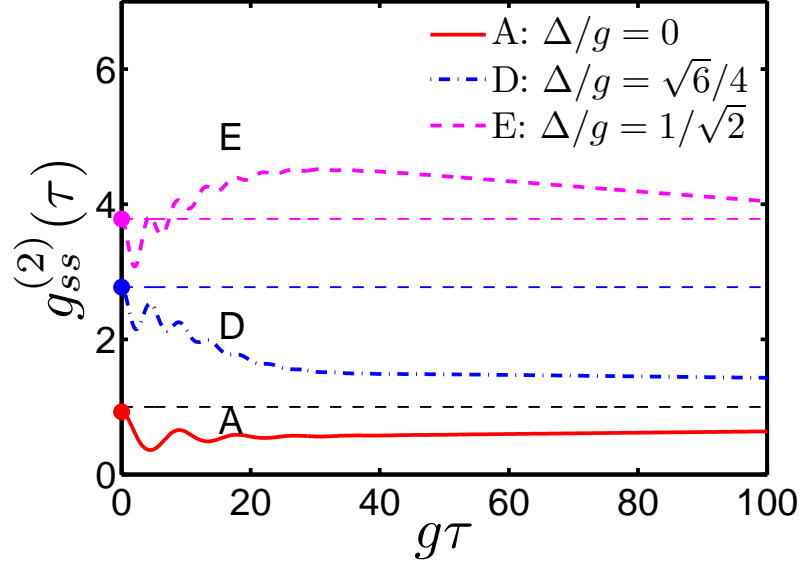


Figure 2.12: Finite time delay intensity correlation function $g_{ss}^{(2)}(\tau)$ for detunings $\Delta/g = 0$ (A), $\sqrt{6}/4$ (D) and $1/\sqrt{2}$ (E). Thin dashed lines indicate the classical bounds (see Eq. 2.37). Labels A, D, E correspond to the same detunings marked in Fig. 2.3 and Fig. 2.11. Parameters are $g/\kappa = 8$, and $\gamma/\kappa = 0.02$.

equations for the amplitudes,

$$\dot{A}_{001} \approx -\frac{\gamma}{2}A_{001}, \quad (2.41)$$

$$\dot{A}_{101} = -i\frac{g}{\sqrt{2}}A_{012} - i\Omega A_{001} - \tilde{\kappa}A_{101}, \quad (2.42)$$

$$\dot{A}_{012} = -i\frac{g}{\sqrt{2}}A_{101} - \tilde{\kappa}A_{012}, \quad (2.43)$$

where we used $\gamma \ll \kappa$ and kept the leading term in Eq. 2.41. We obtain $g_{ss}^{(2)}(\tau)$ by solving these equations for initial conditions determined by the conditional state $|\psi^s\rangle$ after a quantum jump,

$$|\psi^s\rangle = \frac{c_s|\psi\rangle}{||c_s|\psi\rangle||}, \quad (2.44)$$

which is a superposition of states $|001\rangle, |101\rangle, |012\rangle$ (see Appendix A.2 for details),

but in the limit of weak driving consist mainly of $|001\rangle$.

Detection of a photon in the undriven mode implies that the three-wave mixing interaction converted a photon from the driven mode into the undriven mode by simultaneously adding a phonon. The relevant three-level subspace after the jump (see Fig. 2.13) has a similar structure as in the steady state, but the presence of an extra phonon modifies the splitting of the one-photon states $|1'_{\pm}\rangle = (|101\rangle \pm |012\rangle)/\sqrt{2}$ to $\frac{g}{\sqrt{2}}$ (instead of $g/2$ without a phonon). This changes the one-photon resonance

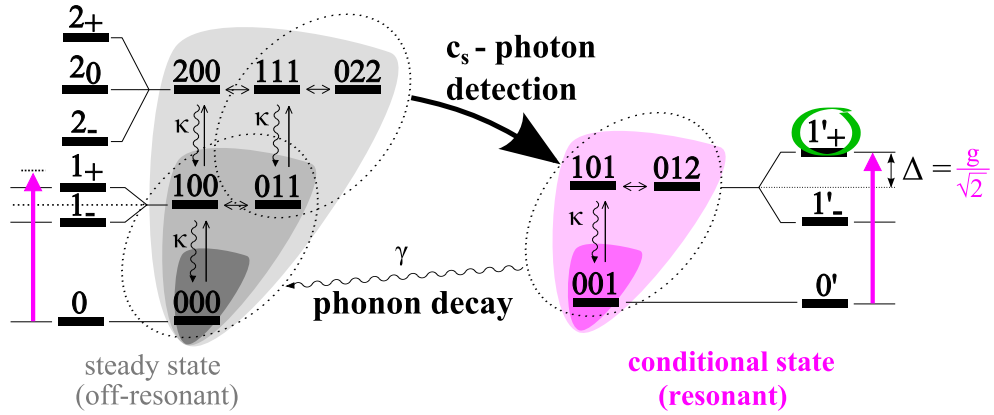


Figure 2.13: Effect of detection of a c_s photon at detuning E ($\Delta/g = \frac{1}{\sqrt{2}}$). In steady state (gray region on left), the drive is far off-resonant. However, after detection of a c_s photon the system jumps into the conditional subspace (pink region on right). Due to the presence of an extra phonon in this subspace, the drive is resonant and the probability to detect a second photon is much higher than in steady state. This increased probability persists as long as the extra phonon, which decays slowly at rate γ .

condition for the drive to $\Delta = \frac{g}{\sqrt{2}}$. Therefore, at this value of the detuning, the process of exciting the system and emitting a single c_s photon is off-resonant; while after the detection of a first c_s photon the system is prepared in $|001\rangle$, bringing it into resonance with the drive. This *enhances* the probability for subsequent excitation and emission of a second c_s photon, increasing the correlation function at finite delay.

The maximum delayed coincidence occurs after a delay of $\tau \sim 1/\kappa$, when the photons have reached the metastable steady state in the conditional subspace with one extra phonon. Eventually, the delayed coincidence returns to its true steady state value of one on the timescale $\tau \sim 1/\gamma$, which is the mechanical decay time of the state $|001\rangle$. The long tails observed for other values of detuning (curves A and D) are also due to the presence of an extra phonon, but in these cases the system remains off-resonant after the initial c_s photon and the effect is less pronounced. Note that the probability to detect a photon from the *driven* mode also increases in the conditional state, so a similar effect is seen in the delayed cross-correlation function $g_{as}^{(2)}(\tau)$, where the photon in the undriven mode is detected first.

2.5 Reaching strong coupling

The nonclassical correlations predicted in this paper require strong optomechanical coupling, $g > \kappa$, as well as sideband resolution, $\omega_m \gg \kappa, \gamma$. While the combination of these conditions has not yet been demonstrated, several experimental efforts are currently directed at reaching this regime. By using micro- and nano-fabricated OMSs such as microtoroids or photonic crystal beams, high frequency mechanical systems with $\omega_m \approx 50$ MHz - 5 GHz can be combined with low loss optical modes, such that the condition $\omega_m \gg \kappa \gg \gamma$ is satisfied [55, 56, 21]. At the same time the mechanical system can already be prepared close to the quantum ground state by working at cryogenic temperatures. In micro-fabricated OMSs, single-photon couplings of about $g/\kappa \approx 0.001$ have been demonstrated [21, 18, 67] The largest value to date of $g/\kappa \approx 0.007$ has been reached in photonic crystal beam resonators [12], where colocalized

optical and vibrational resonances are highly confined to maximize coupling while the surrounding structure is engineered to minimize loss. Conversely, in cold atomic experiments the effective strong OM coupling regime has been reached [48], while sideband resolution remains a challenge [59].

There are several existing proposals for how to meet the challenge of $g/\kappa > 1$ in the photonic crystal beam setup. First, the single-photon optomechanical coupling can be increased by making use of nanoslots in the structure [53, 17] to further localize the electric field at the position of the mechanical mode. This could improve g by a factor of 10 [38]. Second, numerical studies suggest that κ can be further decreased by fine tuning the size and position of the slots in the photonic crystals [45, 62]. Finally, new materials are currently being tested for an overall improvement of the OM properties of nano-fabricated devices [71]. Thus by using these ultrahigh Q photonic crystals or similar designs, an increase of g/κ by a factor of ~ 100 is realistic. Note that once the strong coupling condition has been achieved, the implementation of two or multimode OMSs with adjustable tunneling $2J \sim \omega_m$ can be realized via evanescent field coupling, as has already been demonstrated in the weak coupling regime [55, 21, 28].

2.6 Conclusions

We have studied nonclassical intensity correlations in a driven, near-resonant optomechanical system with one mechanical and two optical modes. In the regime of strong coupling $g > \kappa$, this system allows for nonlinear quantum optics through a resonant three-mode interaction in which the exchange of two photons is mediated by

a phonon. We have identified several different processes that can lead to nonclassical antibunching and delayed bunching, and we have derived a simple analytic model that allows us to describe and interpret photon-photon correlations in this system both at zero and at finite temperature. Our findings will be important as experiments approach the regime of strong OM coupling, and for potential applications of OMSs for quantum information processing. In particular, the long-lived correlation found for the undriven mode raises the intriguing possibility to exploit such a setup as a quantum memory. The generation of heralded single phonons on detection of a photon from the undriven mode may have implications for building OM quantum repeaters and quantum communication devices.

Chapter 3

Optomechanical quantum information processing

3.1 Introduction

Optomechanics describes the radiation pressure interaction between an optical cavity mode and the motion of a macroscopic mechanical object, as it appears, for example, in a Fabry-Pérot cavity with a moveable mirror [32, 41, 3]. First demonstrations of optomechanical (OM) laser cooling [43, 26, 2, 33, 16, 66, 56, 69] have recently attracted significant interest and led to tremendous progress in the development of new fabrication methods and experimental techniques for controlling OM interactions at the quantum level. Apart from ground-state cooling [65, 11], this includes the demonstration of slow light [68, 54], and the coherent interconversion of optical and mechanical excitations [23, 67]. These achievements pave the way for a new type of quantum light-matter interface and give rise to interesting perspec-

tives for novel OM-based quantum technologies. As a solid-state approach, such an all-OM platform would benefit directly from advanced nanofabrication and scalable integrated photonic circuit techniques. At the same time, long mechanical lifetimes comparable to those of atomic systems allow us to combine optical nonlinearities with a stationary quantum memory for light.

In this work we study strong OM coupling effects in *multimode* OM systems (OMSs) and describe how resonant or near-resonant interactions in this setting allow us to exploit the intrinsic nonlinearity of radiation pressure in an optimal way. Our approach is based on the resonant exchange of photons between two optical modes mediated by a single phonon. This resonance induces much stronger nonlinearities than achievable in single-mode OMSs, where nonlinear effects are suppressed by a large mechanical frequency [42, 37, 49, 46]. Consequently, multimode OMSs provide a promising route for accessing the single-photon strong-coupling regime, where the coupling g_0 as well as the mechanical frequency ω_m exceeds the cavity decay rate κ [49]. This regime is within reach of state-of-the-art nanoscale OM devices [11, 21, 10, 18] or analogous cold atom OMSs [29, 8], and here we discuss how strong OM interactions in a multimode setup can be used to generate single photons and to perform controlled gate operations between photonic or mechanical qubits. Combined with very recently developed photon-phonon interfaces and quantum memories based on linearized OM couplings [23, 67, 55], our results provide a basis for efficient OM classical and quantum information processing with applications ranging from photon transistors to quantum repeaters and networks.

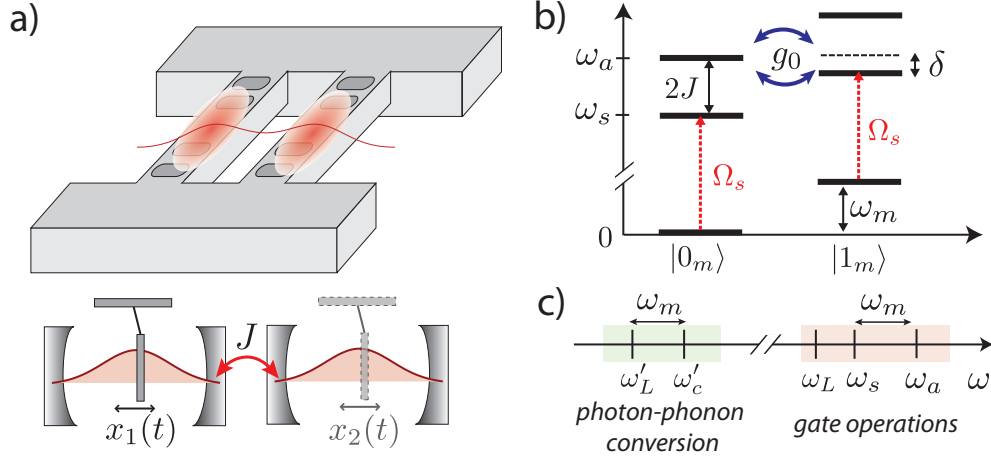


Figure 3.1: a) Setup of two tunnel-coupled OM crystal cavities (see Ref. [21, 11] for more details). b) Level diagram showing the lowest mechanical and optical excitations in a two mode OMS. Resonant coupling ($\delta = 0$) occurs when the tunnel splitting $2J$ between the optical modes is comparable to the mechanical frequency ω_m . c) Different sets of strongly and weakly coupled optical modes and control laser fields can be used for nonlinear interactions ($\omega_s, \omega_a, \omega_L$) and purely linear photon storage and retrieval operations (ω'_c, ω'_L).

3.2 Model

We consider a setup of two tunnel-coupled OMSs [44, 28, 19, 55, 15] as schematically shown in Fig. 3.1, focusing on the OM crystal design [21, 11] as a specific example. Each OMS $i = 1, 2$ is represented by an optical mode of frequency ω_c and a bosonic operator c_i , which is coupled via optical gradient forces to the motion of an isolated mechanical mode b_i with vibrational frequency ω_m^i . The Hamiltonian for this system is ($\hbar = 1$)

$$\begin{aligned}
 H = & \sum_{i=1,2} \omega_m^i b_i^\dagger b_i + \omega_c c_i^\dagger c_i + g_0 c_i^\dagger c_i (b_i + b_i^\dagger) \\
 & - J(c_1^\dagger c_2 + c_1 c_2^\dagger) + \sum_{i=1,2} \Omega_i (c_i e^{i\omega_L t} + \text{H.c.}),
 \end{aligned} \tag{3.1}$$

where J is the tunneling amplitude between the optical modes and g_0 denotes the single-photon OM coupling; Ω_i are the local amplitudes of external control laser fields of frequency ω_L . Below we also consider an additional set of cavity modes and driving fields with frequencies ω'_c and ω'_L , respectively. As indicated in Fig. 3.1(c), we assume these modes to be separated in frequency and used for cooling the mechanical modes [70, 40], and linear photon storage and retrieval operations [23, 67, 72, 1] only.

Apart from the coherent dynamics described by Eq. (3.1), we include dissipation through cavity decay and mechanical damping and model the evolution of the system density operator ρ by a master equation (ME)

$$\dot{\rho} = -i[H, \rho] + \sum_i \kappa \mathcal{D}[c_i] \rho + \mathcal{L}_\gamma \rho, \quad (3.2)$$

where $\mathcal{D}[c]\rho = 2c\rho c^\dagger - \{c^\dagger c, \rho\}_+$, and $\mathcal{L}_\gamma = \sum_i \frac{\gamma}{2}(N_{\text{th}} + 1)\mathcal{D}[b_i] + \frac{\gamma}{2}N_{\text{th}}\mathcal{D}[b_i^\dagger]$. Here, κ is the optical field decay rate, $\gamma = \omega_m/Q$ the mechanical damping rate for a quality factor Q and $N_{\text{th}} = (e^{\hbar\omega_m/k_B T} - 1)^{-1}$ the mechanical equilibrium occupation number for temperature T . Below we identify $\Gamma_m = \frac{\gamma}{2}(3N_{\text{th}} + \frac{1}{2})$ as the characteristic decoherence rate for mechanical qubit states¹.

3.3 Resonant strong-coupling optomechanics

We focus on the strong coupling regime $\omega_m, g_0 \gg \kappa, \Gamma_m$, and our main goal is to show how the multimode OMS described by Eq. (3.1) can be used for implementing controlled interactions between qubits encoded in photonic or phononic degrees of freedom. To illustrate this we first consider a single mechanical resonator,

¹ Γ_m corresponds to the initial decoherence rate of a phonon superposition $(|0_m\rangle + |1_m\rangle)/\sqrt{2}$.

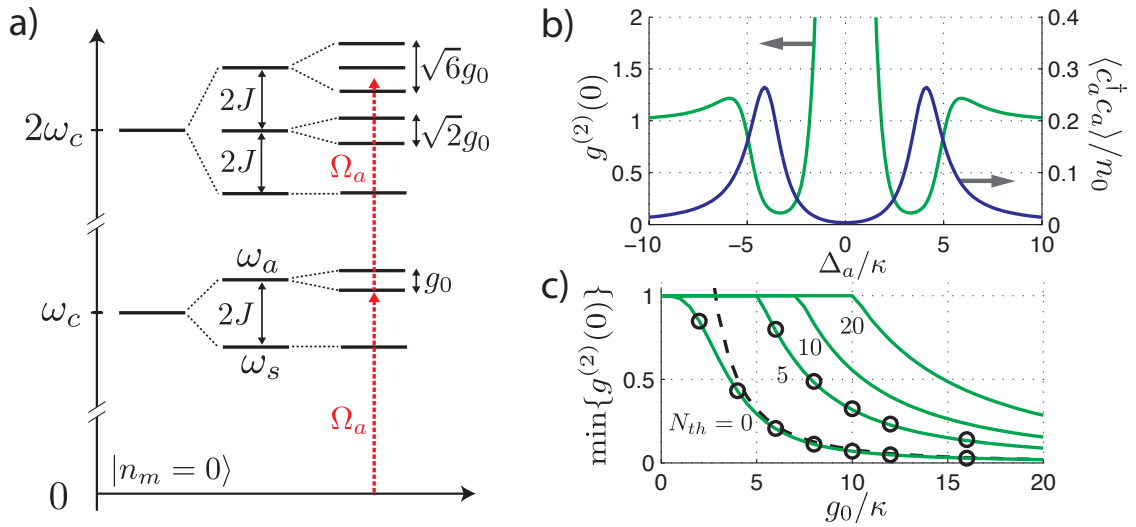


Figure 3.2: a) Energy level diagram of a resonantly coupled OMS, $\delta = 2J - \omega_m = 0$, and for a single mechanical mode in the ground state. b) Excitation spectrum and $g^{(2)}(0)$ for a weak coherent field exciting the c_a mode, where $g_0/\kappa = 8$ and $n_0 = \Omega_a^2/\kappa^2$. c) Minimal value of $g^{(2)}(0)$ as a function of the OM coupling strength g_0 and for different values of N_{th} . The analytical results (solid lines) given in the text are in good agreement with exact numerics (circles). The dashed line shows the asymptotic scaling $\sim 8\kappa^2/g_0^2$ at zero temperature.

$b \equiv b_1$, $\omega_m \equiv \omega_m^1$. We introduce symmetric and antisymmetric optical modes $c_{s,a} = (c_1 \pm c_2) / \sqrt{2}$ with eigenfrequencies $\omega_{s,a}$ split by $2J$. Further, we assume that $\omega_m \sim 2J \gg g_0, \kappa, |\delta|$, where $\delta = 2J - \omega_m$ (see Fig. 3.1(b)). This condition can be achieved in nanoscale OMSs where $\omega_m \sim \text{GHz}$ [21, 11, 10, 18] and a matching tunnel splitting can be designed by appropriately adjusting the spacing between the cavities [21, 28]. In this regime we can make a rotating wave approximation with respect to the large frequency scale $\omega_m \sim 2J$ and after changing into a frame rotating with ω_L we obtain [28]

$$H = -\Delta_s c_s^\dagger c_s - \Delta_a c_a^\dagger c_a + \omega_m b^\dagger b + \frac{g_0}{2} (c_a c_s^\dagger b^\dagger + c_a^\dagger c_s b) + H_\Omega(t). \quad (3.3)$$

Here $\Delta_{s,a} = \omega_L - \omega_{s,a}$ are the detunings of the driving field from the c_s and c_a mode, respectively, and $H_\Omega(t) = \sum_{\eta=s,a} (\Omega_\eta(t) c_\eta + \text{H.c.})$ accounts for the external driving fields with slowly varying amplitudes $\Omega_{s,a}(t) = (\Omega_1(t) \pm \Omega_2(t)) / \sqrt{2}$.

The two-mode OM coupling in Eq. (3.3) describes photon transitions between the energetically higher mode c_a to the lower mode c_s , while simultaneously absorbing or emitting a phonon. For $(\Delta_s - \Delta_a - \omega_m) = \delta = 0$, this leads to a resonant interaction between states $|n_a, n_s, n_m\rangle$ and $|n_a - 1, n_s + 1, n_m + 1\rangle$, where n_a , n_s and n_m label the occupation numbers of the two optical modes and the mechanical mode, respectively. In analogy to atomic cavity quantum electrodynamics (QED) [50], the nonlinear scaling of the corresponding transition amplitudes $\frac{g_0}{2} \sqrt{n_a(n_s + 1)(n_m + 1)}$ results in an anharmonic level diagram as shown in Fig. 3.2(a). If g_0 exceeds the cavity linewidth κ , one and two photon transitions can be spectrally resolved, indicating the onset of strong single-photon nonlinearities.

3.4 An OM single-photon source

As a potential first application of the nonlinear OM interaction we discuss the use of the OMS as a single-photon source, which is characterized by a vanishing equal time two-photon correlation function $g^{(2)}(0)$. In Fig. 3.2(b) we plot the excitation spectrum $\langle c_a^\dagger c_a \rangle$ and $g^{(2)}(0) = \langle c_a^\dagger c_a^\dagger c_a c_a \rangle / \langle c_a^\dagger c_a \rangle^2$, for the case where only the c_a mode is weakly driven. Around the single-photon resonances $\Delta_a = \pm g_0/2$ we observe strong anti-bunching $g^{(2)}(0) < 1$ as a clear signature of non-classical photon statistics. To quantify this effect we assume that $\Gamma_m \ll \kappa$, which allows us to treat subspaces connected to different $|n_m\rangle$ separately. For weak driving fields $\Omega_a \ll \kappa$, the system dynamics can then be restricted to the six states $|0_a, 0_s, n_m\rangle, |1_a, 0_s, n_m\rangle, |0_a, 1_s, n_m + 1\rangle, |2_a, 0_s, n_m\rangle, |1_a, 1_s, n_m + 1\rangle, |0_a, 2_s, n_m + 2\rangle$ and we calculate the relevant occupation probabilities $p_{1,0,n_m}$ and $p_{2,0,n_m}$ to leading order in Ω_a [9]. We obtain

$$p_{1,0,n} = \left| \frac{4\Omega_a d}{X_n} \right|^2, \quad p_{2,0,n} = 8 \left| \frac{\Omega_a^2 (8d^2 - g_0^2)}{(X_n(2X_n - g_0^2))} \right|^2, \quad (3.4)$$

where $d = \Delta_a - i\kappa$ and $X_n = d^2 - g_0^2(n+1)$. By taking the appropriate thermal averages, $\langle n_a \rangle = \sum_n \zeta_n p_{1,0,n}$ and $g^{(2)}(0) = 2 \sum_n \zeta_n p_{2,0,n} / \langle n_a \rangle^2$, where $\zeta_n = (1 - e^{-\beta\hbar\omega_m})e^{-\beta\hbar\omega_m n}$ and $\beta^{-1} = k_B T$, the two photon correlation function can be evaluated for arbitrary temperatures T .

In Fig. 3.2(c) we plot the minimal value of $g^{(2)}(0)$ as a function of the coupling strength g_0 and for different N_{th} . As the OM coupling increases we find that for $T = 0$ the minimum of the correlation function scales as $\min_{\Delta_a} \{g^{(2)}(0)\} \simeq 8\kappa^2/g_0^2$. This demonstrates an improved scaling over off-resonant photon blockade effects in single-mode OMSs, where for large ω_m only a small reduction $g^{(2)}(0) \simeq 1 - g_0^2/(\kappa\omega_m)$ can

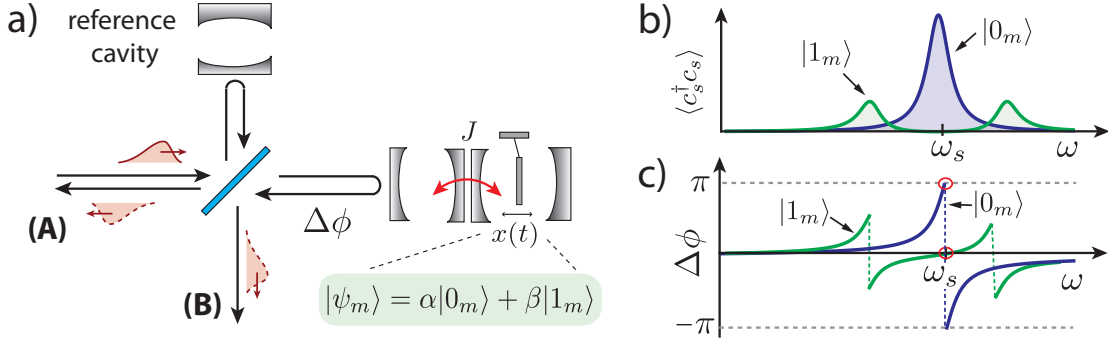


Figure 3.3: a) An incoming photon in port (A) passes through the interferometric setup and leaves through port (A) or (B), depending on the phase shift $\Delta\phi$ acquired upon reflection from the two-mode OMS. b), c) For a mechanical system in state $|0_m\rangle$, the OMS exhibits a single resonance at ω_s ($\Delta\phi = \pi$), while for state $|1_m\rangle$ the resonance splits by $g_0 \gg \kappa$ and the photon does not enter the cavity ($\Delta\phi = 0$).

be obtained [49]. Since the positions of the single and two-photon resonances depend explicitly on the mechanical state $|n_m\rangle$, finite temperature degrades the quality of the single-photon source. Nevertheless, with increasing coupling strength the antibunching effect becomes surprisingly robust and when combined with cooling cycles to achieve $\langle n_m \rangle \sim 1$ [11], allows the operation of OM single-photon sources even at environmental temperatures of a few Kelvin.

3.5 Single-phonon single-photon transistor

Given the ability to generate single photons, Fig. 3.3 illustrates a basic scheme for using the same resonant OMS to implement a two-qubit gate [20]. First, we assume that the state of a control photon is mapped onto a mechanical superposition state $\alpha|0_m\rangle + \beta|1_m\rangle$. This can be achieved with conventional cooling followed by photon-phonon conversion techniques using linearized OM interactions with an aux-

iliary mode ω'_c (see Fig. 3.1(c)). Next, a single target photon of central frequency $\sim \omega_s$ is sent through the interferometric setup as described in Fig. 3.3. If the mechanical mode is in the state $|0_m\rangle$, the incoming photon couples to a single resonant state $|0_a, 1_s, 0_m\rangle$ (see Fig. 3.1(b)), such that it enters the cavity and picks up a phase before being reflected. Instead, if the mechanical resonator is in the state $|1_m\rangle$, the resonant coupling between $|0_a, 1_s, 1_m\rangle$ and $|1_a, 0_s, 0_m\rangle$ splits the cavity resonance, and for $g_0 > \kappa$ the photon is reflected without a phase shift. Under ideal conditions, the final result is an entangled state

$$|\psi\rangle = \alpha|0_m, 1_A, 0_B\rangle + \beta|1_m, 0_A, 1_B\rangle, \quad (3.5)$$

where A and B are the two ports of the interferometer. This state can be converted back into an entangled state between the initial control and target photon.

Assuming that the storage and retrieval of the control photon can be achieved with high fidelity, the error for producing the entangled state (3.5) with $\alpha = \beta = 1/\sqrt{2}$ is approximately given by

$$\epsilon \approx \frac{4\kappa^2}{g_0^2} + \frac{1}{(\tau_p \kappa)^2} + \tau_p \Gamma_m, \quad (3.6)$$

where τ_p is the duration of the single-photon pulse. The individual contributions in Eq. (3.6) arise from an imperfect photon reflection, the finite spectral width of the photon pulse, and mechanical decoherence, respectively. A minimal error is achieved for $\tau_p^{-1} \approx \sqrt[3]{\kappa^2 \Gamma_m}$ where we obtain $\epsilon \approx \max\{4\kappa^2/g_0^2, \sqrt[3]{\Gamma_m^2/\kappa^2}\}$. Assuming an OM crystal device with $\omega_m/(2\pi) = 4$ GHz and $Q = 10^5$ as discussed in Ref. [11], but with an improved OM coupling $g_0/(2\pi) = 50$ MHz and a lower decay rate $\kappa/(2\pi) = 5$ MHz, we obtain gate errors $\epsilon \approx 0.1$ for environmental temperatures around $T \approx 100$ mK.

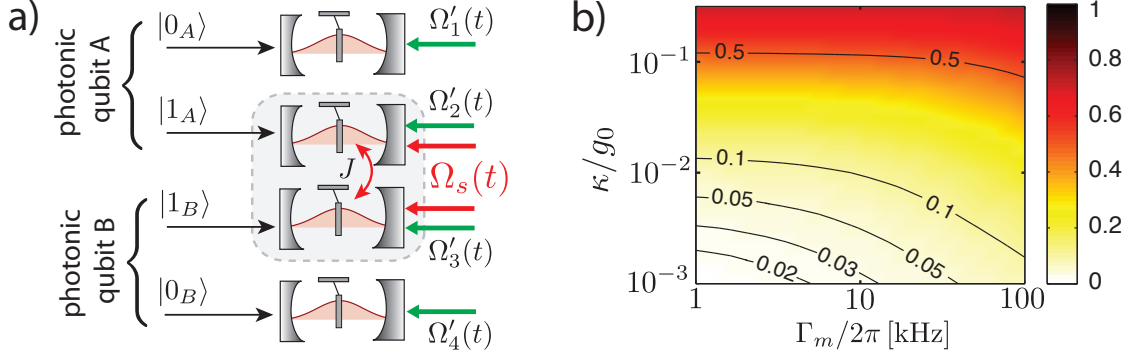


Figure 3.4: a) OM quantum memory, where ‘path-encoded’ photonic qubits are stored in long-lived mechanical states using tunable linearized OM interactions $\sim \Omega'_i(t)$. Deterministic gate operation between stationary qubits are implemented by a controlled phonon-phonon interaction $\sim \Omega_s(t)$ as described in the text. b) The total error ϵ_g for implementing a controlled phase gate between two photonic qubits is minimized with respect to Δ_s and plotted as a function of κ and Γ_m (see text). The parameters for this plot are $g_0/(2\pi) = 50$ MHz, $\gamma/(2\pi) = 4$ kHz, $\alpha = 1$ and $g_0/\delta = 1/3$.

3.6 Phonon-phonon interactions

Finally, we consider the possibility to perform a controlled gate operation between two qubits stored in long-lived mechanical modes. Our approach is depicted in Fig. 3.4(a), and combines the long coherence times of an OM quantum memory [23, 67, 72, 1] with the practical utility of exploiting interactions between stationary phononic qubits. We focus on the limit $\Gamma_m \ll \kappa$, and assume that optical (e.g. ‘path encoded’) qubits are first mapped onto long-lived states $|0_m\rangle$ and $|1_m\rangle$ of two or more mechanical modes. The OM coupling is then employed to generate nonlinear interactions between the phonons only.

We consider nonlinear interactions between two mechanical modes b_1 and b_2 described by Eq. (3.1), detuned from resonance such that $g_0 < |(2J - \omega_m^i)|$ and direct transitions between photons and phonons are suppressed. To obtain the effective

phonon-phonon interactions, we first diagonalize H to second order in $\xi_i = g_0/(2J - \omega_m^i)$ with the transformation $H \rightarrow e^{iS} H e^{-iS}$, where $S = \frac{i}{2}(c_s^\dagger c_a (\xi_1 b_1^\dagger - \xi_2 b_2^\dagger) - \text{H.c.})$. This yields $H = H_0 + H_g + H_\Omega(t)$, where $H_0 = -\Delta_s c_s^\dagger c_s - \Delta_a c_a^\dagger c_a + \sum_i \omega_m^i b_i^\dagger b_i$,

$$H_g = \frac{g_0}{4} [(c_s^\dagger c_s + 1) c_a^\dagger c_a (\xi_1 + \xi_2) + (c_a^\dagger c_a - c_s^\dagger c_s) \mathcal{N}_b], \quad (3.7)$$

and we have neglected small corrections to the driving Hamiltonian $H_\Omega(t)$. The phonon operator in Eq. (3.7) is given by $\mathcal{N}_b = \xi_1 b_1^\dagger b_1 + \xi_2 b_2^\dagger b_2 - (\xi_1 + \xi_2)(b_1^\dagger b_2 + b_2^\dagger b_1)/2$. For simplicity we focus on symmetric detuning, $\omega_m^{1,2} = 2J \mp \delta$, where $\mathcal{N}_b = \frac{g_0}{\delta}(b_1^\dagger b_1 - b_2^\dagger b_2)$. The transformation also modifies the dissipative terms in the Eq. (3.2); most importantly, we find an optically-induced decay channel for the mechanical modes, $\mathcal{L}_\gamma \rightarrow \mathcal{L}_\gamma + \kappa g_0^2/(4\delta^2) \mathcal{D}[c_s(b_1 + b_2)]$.

We assume that only the c_s mode is weakly driven by a slowly-varying control field $\Omega_s(t)$. In this case the c_a mode remains unpopulated and we neglect it. Next, we shift the driven mode, $c_s \rightarrow \alpha + c_s$, by the classical amplitude α , yielding an effective ME for c_s , b_1 and b_2 . Finally, we adiabatically eliminate the c_s mode, valid in the limit $|\alpha| \sim \mathcal{O}(1)$ and $(g_0^2|\alpha|/4\delta) \ll |\Delta_s + i\kappa|$, to obtain an effective ME for the mechanical modes (see Appendix B for more details),

$$\begin{aligned} \dot{\rho}_m = & -i[H_m + \Lambda(b_1^\dagger b_1 - b_2^\dagger b_2)^2, \rho_m] + \mathcal{L}_\gamma \rho_m \\ & + \Gamma_\phi \mathcal{D}[(b_1^\dagger b_1 - b_2^\dagger b_2)] \rho_m + \frac{\gamma'}{2} \sum_i \mathcal{D}[b_i] \rho_m. \end{aligned} \quad (3.8)$$

Here, $\gamma' = \kappa|\alpha|^2 g_0^2/(2\delta^2)$, and the phonon-phonon interaction and the phonon dephasing rate are given by

$$\Lambda = \frac{g_0^4 |\alpha|^2 \Delta_s}{16\delta^2 (\Delta_s^2 + \kappa^2)}, \quad \Gamma_\phi = \frac{g_0^4 |\alpha|^2 \kappa}{16\delta^2 (\Delta_s^2 + \kappa^2)}. \quad (3.9)$$

The effective Hamiltonian in Eq. (3.8) describes a phonon nonlinearity with a tunable strength $\Lambda(t) \sim |\alpha(t)|^2$. The relevant cross-coupling is given by

$$H_{\text{int}} \simeq 2\Lambda b_1^\dagger b_1 b_2^\dagger b_2, \quad (3.10)$$

and when acting for a time $t_g = \pi/(2\Lambda)$, this Hamiltonian implements a controlled-phase gate between two qubits encoded in states $|0_m\rangle$ and $|1_m\rangle$. During this time, phonons experience intrinsic and optically-induced decoherence as seen in Eq. (3.8).

In Fig. 3.4, we plot the resulting gate error $\epsilon_g = 1 - \langle \psi_0 | \rho_m(t_g) | \psi_0 \rangle$ for an initial state $|\psi_0\rangle = \frac{1}{2}(|0_m\rangle + |1_m\rangle)^{\otimes 2}$ optimized with respect to Δ_s . Using the total decoherence rate of this state, $\Gamma_{\text{decoh}} = 2\Gamma_m + \Gamma_\phi + \gamma'/2$, we find that $\epsilon_g \propto \Gamma_{\text{decoh}}/\Lambda$ is minimized for $|\Delta_s| \simeq g_0/2$, where $\epsilon_g \propto 4(\kappa/g_0)$. While this scaling with g_0 is weaker than for a gate based on photon reflection (see Eq. (3.6)), the ability to perform a gate between stationary qubits represents an important advantage of this approach.

3.7 Conclusions

We have described single-photon and single-phonon nonlinear effects in strongly coupled multimode OMSs. We have shown how induced nonlinearities on or near resonance can be used for controlled quantum gate operations between flying optical or stationary phononic qubits. Our results provide a realistic route towards the quantum nonlinear regime of OMSs, and a framework for future OM information processing applications.

Chapter 4

Heralded Quantum Gates with Integrated Error Detection in Optical Cavities

4.1 Introduction

From [6]

Chapter 5

Long-distance entanglement distribution using individual atoms in optical cavities

5.1 Introduction

From [5]

Chapter 6

Heisenberg-Limited Atom Clocks Based on Entangled Qubits

6.1 Introduction

From [31]

Chapter 7

A quantum network of clocks

7.1 Introduction

From [34]

Chapter 8

Entangling collective Rydberg excitations of remote atomic ensembles

8.1 Introduction

From [1]

Appendix A

Appendices for Chapter 2

A.1 Derivation of reflected mode operator

We obtain the reflected mode operator c_R using input-output relations for a two-sided cavity. By assuming that the two endmirrors have the same transmittivity ($\propto \kappa$), we can write the input-output relation for cavity mode c_a on the driven mirror as

$$c_{a,\text{out}} = \sqrt{\kappa}c_a - c_{a,\text{in}}, \quad (\text{A.1})$$

where $c_{a,\text{in}} = -i\frac{\Omega}{\sqrt{\kappa}}$ is the incoming field operator on the mirror and $c_{a,\text{out}}$ is the output field operator. For direct comparison with c_a we divide by $\sqrt{\kappa}$ and define the reflection mode operator as $c_R \equiv c_{a,\text{out}}/\sqrt{\kappa} = c_a + i\frac{\Omega}{\kappa}$.

A.2 Analytic model

In this appendix we provide the analytic solutions used to calculate one- and two-time correlation functions in steady state. First, one-time correlations are calculated from the steady state solutions of Eqs. (2.13–2.18). We set the time derivatives to zero and solve the equations iteratively, order by order in the weak drive. This procedure yields

$$\bar{A}_{000} \approx 1, \quad (\text{A.2})$$

$$\bar{A}_{100} = -i\alpha \frac{1}{1+4x^2}, \quad (\text{A.3})$$

$$\bar{A}_{011} = -\alpha \frac{2x}{1+4x^2}, \quad (\text{A.4})$$

$$\bar{A}_{200} = -\frac{\alpha^2}{\sqrt{2}} \frac{1+2x^2}{(1+4x^2)(1+6x^2)}, \quad (\text{A.5})$$

$$\bar{A}_{111} = i\alpha^2 \frac{2x}{(1+4x^2)(1+6x^2)}, \quad (\text{A.6})$$

$$\bar{A}_{022} = \alpha^2 \frac{4x^2}{(1+4x^2)(1+6x^2)}, \quad (\text{A.7})$$

where $\alpha = \Omega/\tilde{\kappa}$ ($|\alpha|^2 \ll 1$), $x = g/(4\tilde{\kappa})$ and $\tilde{\kappa} = \kappa - i\Delta$. Using these amplitudes, we can express all equal time averages. The mean photon numbers are

$$\bar{n}_a = |\bar{A}_{100}|^2, \quad (\text{A.8})$$

$$\bar{n}_s = |\bar{A}_{011}|^2, \quad (\text{A.9})$$

$$\bar{n}_R = \left| \bar{A}_{100} + i\frac{\Omega}{\kappa} \right|^2, \quad (\text{A.10})$$

and the photon-photon correlation functions are

$$g_{aa}^{(2)}(0) = \frac{2|\bar{A}_{200}|^2}{|\bar{A}_{100}|^4}, \quad (\text{A.11})$$

$$g_{ss}^{(2)}(0) = \frac{2|\bar{A}_{022}|^2}{|\bar{A}_{011}|^4}, \quad (\text{A.12})$$

$$g_{RR}^{(2)}(0) = \frac{\left| -\left(\frac{\Omega}{\kappa}\right)^2 + 2i\frac{\Omega}{\kappa}\bar{A}_{100} + \sqrt{2}\bar{A}_{200} \right|^2}{\left| i\frac{\Omega}{\kappa} + \bar{A}_{100} \right|^4}. \quad (\text{A.13})$$

To leading order in κ/g these yield Eqs. (2.19–2.24).

At finite temperature we calculate steady state amplitudes within each phonon subspace n similarly in the ansatz of Eq. 2.26. Using the notation $R_\kappa(\omega)$ introduced in Section 2.3.2, the steady state amplitudes within the subspace with n phonons in the optical groundstate are

$$|\bar{A}_{10n}|^2 = \frac{\Omega^2 \sqrt{R_\kappa(0)}}{R_\kappa\left(\frac{g}{2}\sqrt{n+1}\right)}, \quad (\text{A.14})$$

$$|\bar{A}_{01n+1}|^2 = \frac{\Omega^2 g^2 (n+1)}{4R_\kappa\left(\frac{g}{2}\sqrt{n+1}\right)}, \quad (\text{A.15})$$

$$|\bar{A}_{20n}|^2 = \frac{\Omega^4 R_\kappa(g/\sqrt{8})}{R_\kappa\left(g\sqrt{(2n+1)/8}\right) R_\kappa\left(\frac{g}{2}\sqrt{n+1}\right)}, \quad (\text{A.16})$$

$$|\bar{A}_{02n+2}|^2 = \frac{\Omega^4 g^4 (n+1)(n+2)}{32R_\kappa\left(g\sqrt{(2n+1)/8}\right) R_\kappa\left(\frac{g}{2}\sqrt{n+1}\right)}. \quad (\text{A.17})$$

Two-time correlation functions are calculated similarly, using the conditional state after a jump (see Eqs. (2.39) and (2.44)) as the initial condition. For example the unnormalized state after detection of a photon in the c_a mode is $c_a|\psi\rangle = \bar{A}_{100}|000\rangle + \sqrt{2}\bar{A}_{200}|100\rangle + \bar{A}_{111}|011\rangle$. We solve Eqs. (2.13–2.15) for the amplitudes with this state as initial condition. The finite delay correlation of the driven mode is

$$g_{aa}^{(2)}(\tau) = \frac{|A_{100}(\tau)|^2}{|\bar{A}_{100}|^4}. \quad (\text{A.18})$$

in good agreement with the numerics. The correlation of the undriven mode $g_{ss}^{(2)}(\tau)$ is calculated similarly. The unnormalized state after detection in the c_s mode is $c_s|\psi\rangle = \bar{A}_{011}|001\rangle + \bar{A}_{111}|101\rangle + \sqrt{2}\bar{A}_{022}|012\rangle$. Using this as the initial condition we solve Eqs. (2.41–2.43) for the amplitudes in the conditional state. In the limit of $\gamma \ll \kappa$ we obtain

$$g_{ss}^{(2)}(\tau) = \frac{|A_{012}(\tau)|^2}{|\bar{A}_{011}|^4}. \quad (\text{A.19})$$

Appendix B

Appendices for Chapter 3

B.1 Phonon nonlinearities

In Eq. (8) in the main text we have derived an effective master equation (ME) to describe the nonlinear interaction between two phonon modes. In the following we present an alternative, more rigorous, approach, which illustrates the individual approximations made in the derivation of the effective phonon nonlinearity in more detail. We first consider only a single mechanical mode, e.g. $b \equiv b_1$, which also allows us more easily to compare the results with exact numerical calculations of the full model.

B.1.1 Model

We start with the full ME for the two optical modes coupled to a single resonator mode, which in the frame of the driving frequency ω_L can be written as

$$\dot{\rho} = -i[H_0 + H_g + H_\Omega(t), \rho] + \mathcal{L}_{\text{diss}}\rho. \quad (\text{B.1})$$

Here

$$H_0 = \omega_m b^\dagger b - \Delta_s c_s^\dagger c_s - \Delta_a c_a^\dagger c_a, \quad (\text{B.2})$$

and

$$H_g = \frac{g_0}{2} (c_a c_s^\dagger b^\dagger + c_a^\dagger c_s b), \quad (\text{B.3})$$

are the free evolution and the OM coupling, respectively, $H_\Omega(t) = i\Omega_s(t)(c_s^\dagger - c_s)$ is the driving field for the symmetric mode with slowly varying amplitude $\Omega_s(t)$ and

$$\mathcal{L}_{\text{diss}}\rho = \sum_{\eta=s,a} \kappa \mathcal{D}[c_\eta]\rho + \frac{\gamma}{2} \mathcal{D}_{\text{th}}[b]\rho, \quad (\text{B.4})$$

accounts for dissipation. Here we have defined the superoperator $\mathcal{D}_{\text{th}}[b] = (N_{\text{th}} + 1)\mathcal{D}[b] + N_{\text{th}}\mathcal{D}[b^\dagger]$ to describe the coupling to a thermal bath.

B.1.2 Displaced frame

In contrast to the approach outlined in the main text, we now start our analysis with a unitary displacement $U(t)c_sU^\dagger(t) = c_s + \alpha(t)$ where the classical cavity field $\alpha(t)$ obeys

$$\dot{\alpha}(t) = (i\Delta_s - \kappa)\alpha(t) + \Omega_s(t). \quad (\text{B.5})$$

This unitary transformation eliminates the classical driving field and in the new frame the resulting ME can be written as

$$\dot{\rho} = -i[H_{\text{lin}} + H_g, \rho] + \mathcal{L}_{\text{diss}}\rho, \quad (\text{B.6})$$

where $H_\Omega(t)$ has disappeared, but the linear part of the Hamiltonian now contains an additional coupling between the resonator and the anti-symmetric cavity mode,

$$H_{\text{lin}} = H_0 + G(t)c_a b^\dagger + G^*(t)c_a^\dagger b, \quad (\text{B.7})$$

where $G(t) = g_0\alpha(t)/2$. Note that ME (B.6) is still exact and we will use this equation for our exact numerics below.

B.1.3 Hybridized modes

To proceed, we assume that $\alpha(t)$ is constant or slowly varying on the timescale set by the detunings $|\Delta_a + \omega_m^i|$. This allows us to write H_{lin} in its adiabatic eigenbasis

$$H_{\text{lin}} = -\Delta_s c_s^\dagger c_s - \tilde{\Delta}_a C^\dagger C + \tilde{\omega}_m B^\dagger B, \quad (\text{B.8})$$

where the C and B are bosonic operators for the hybridized mechanical and optical modes and $\tilde{\Delta}_a$ and $\tilde{\omega}_m$ are the new eigenfrequencies of H_{lin} for a given $G \equiv G(t)$. We obtain

$$C = \cos(\theta)c_a - \sin(\theta)b, \quad (\text{B.9})$$

$$B = \cos(\theta)b + \sin(\theta)c_a, \quad (\text{B.10})$$

where $\tan(2\theta) = -2|G|/\delta$ and $\delta = -(\Delta_a + \omega_m) = 2J - \omega_m - \Delta_s$. The shifted frequencies are given by

$$-\tilde{\Delta}_a = -\Delta_a - \frac{1}{2} \left(\delta - \sqrt{\delta^2 + 4|G|^2} \right), \quad (\text{B.11})$$

$$\tilde{\omega}_m = \omega_m - \frac{1}{2} \left(\delta + \sqrt{\delta^2 + 4|G|^2} \right). \quad (\text{B.12})$$

We see that by slowly increasing the classical control field $\alpha(t)$, the mechanical mode b is adiabatically converted into a polaronic mode B . For small mixing angles θ the mode still retains its mechanical character, while the finite photonic component is responsible for inducing an effective nonlinearity.

In terms of the hybridized mode operators the dissipative terms can be written as

$$\begin{aligned} \mathcal{L}_{\text{diss}} \simeq & \kappa \mathcal{D}[c_s] + \kappa \cos^2(\theta) \mathcal{D}[C] + \frac{\gamma}{2} \sin^2(\theta) \mathcal{D}_{\text{th}}[C] \\ & + \frac{\gamma}{2} \cos^2(\theta) \mathcal{D}_{\text{th}}[B] + \kappa \sin^2(\theta) \mathcal{D}[B]. \end{aligned} \quad (\text{B.13})$$

In particular, we identify an additional optical decay channel with rate $\gamma' = 2\kappa \sin^2(\theta)$ for the B mode. In the following we define as

$$\tilde{\mathcal{L}}_\gamma = \frac{\gamma}{2} \cos^2(\theta) \mathcal{D}_{\text{th}}[B] + \frac{\gamma'}{2} \mathcal{D}[B], \quad (\text{B.14})$$

the modified mechanical dissipation Liouvillian. Note that in Eq. (B.13) we have already neglected cross-terms between C and B^\dagger . This is valid in the parameter regime considered below, where κ is small compared to the splitting of these two modes.

Finally, we also express the nonlinear interaction H_g in terms of the hybridized modes and write the result as

$$H_g = H_g^{(1)} + H_g^{(2)} + H'_g. \quad (\text{B.15})$$

Here, the first term is the one of interest

$$H_g^{(1)} = \frac{g_0}{4} \sin(2\theta) (c_s + c_s^\dagger) B^\dagger B, \quad (\text{B.16})$$

and describes the coupling of the c_s mode to the number operator of the B mode.

The second term is given by

$$H_g^{(2)} = -\frac{g_0}{2} \sin^2(\theta) (B c_s^\dagger C^\dagger + B^\dagger c_s C), \quad (\text{B.17})$$

and leads to additional corrections. However, for small θ this term is small compared to $H_g^{(1)}$. It can be further reduced if $|\Delta_s - \delta| \gg \Delta_s$. Finally, the last term contains

interactions

$$H'_g = \frac{g_0}{2} \cos^2(\theta) (C c_s^\dagger B^\dagger + C^\dagger c_s B) - \frac{g_0}{4} \sin(2\theta) (c_s + c_s^\dagger) C^\dagger C, \quad (\text{B.18})$$

which can be neglected when either the c_s or the C mode are in the vacuum state.

B.1.4 Adiabatic elimination of the cavity mode

Our goal is now to derive an effective ME for the mechanical degrees of freedom only. To do so, we write the full ME as

$$\dot{\rho} = (\mathcal{L}_0 + \mathcal{L}_1) \rho, \quad (\text{B.19})$$

where

$$\mathcal{L}_0 \rho = -i[H_{\text{lin}} + H'_g, \rho] + \mathcal{L}_{\text{diss}} \rho, \quad (\text{B.20})$$

and

$$\mathcal{L}_1 \rho = -i[H_g^{(1)} + H_g^{(2)}, \rho]. \quad (\text{B.21})$$

The dynamics of \mathcal{L}_0 does not excite the cavity modes, and therefore, in the limit where $\tilde{g} = g_0 \sin(2\theta)/4 \rightarrow 0$ (either g_0 is small or the mixing angle θ is small) the density operator can to a good approximation be written as $\rho(t) = \rho_m(t) \otimes \rho_c^0$, where ρ_c^0 is the vacuum state of the c_s and the C mode. To account for the effects of a small $\mathcal{L}_1 \sim \tilde{g}$ up to second order in perturbation theory we define a projection operator onto this subspace,

$$\mathcal{P} \rho = \text{Tr}_c\{\rho\} \otimes \rho_c^0, \quad (\text{B.22})$$

and its complement $\mathcal{Q} = \mathbb{1} - \mathcal{P}$. Then

$$\mathcal{P} \dot{\rho} = \mathcal{P} \mathcal{L}_0 \mathcal{P} \rho + \mathcal{P} \mathcal{L}_1 \mathcal{Q} \rho, \quad (\text{B.23})$$

$$\mathcal{Q} \dot{\rho} = \mathcal{Q} (\mathcal{L}_0 + \mathcal{L}_1) \mathcal{Q} \rho + \mathcal{Q} \mathcal{L}_1 \mathcal{P} \rho. \quad (\text{B.24})$$

Up to second order in \tilde{g} we can formally integrate the equation for $\mathcal{Q}\rho$ and obtain

$$\mathcal{P}\dot{\rho}(t) \simeq \mathcal{P}\mathcal{L}_0\mathcal{P}\rho(t) + \mathcal{P}\mathcal{L}_1 \int_0^\infty d\tau \mathcal{Q}e^{\mathcal{L}_0\tau} \mathcal{Q}\mathcal{L}_1\mathcal{P}\rho(t). \quad (\text{B.25})$$

We define by $\rho_m(t) = \text{Tr}_c\{\mathcal{P}\rho(t)\}$ the reduced density operator of the mechanical mode and write the final result as

$$\dot{\rho}_m(t) = (\mathcal{L}_m^{(0)} + \mathcal{L}_m^{(1)} + \mathcal{L}_m^{(2)}) \rho_m(t). \quad (\text{B.26})$$

The first term describes the linear part of the dynamics

$$\mathcal{L}_m^{(0)} \rho_m = -i[\tilde{\omega}_m B^\dagger B, \rho_m] + \tilde{\mathcal{L}}_\gamma \rho_m, \quad (\text{B.27})$$

with a modified frequency and modified decay rates for the B mode. The other two terms are given by

$$\mathcal{L}_m^{(1)} \rho_m = - \int_0^\infty d\tau \text{Tr}_c\{[H_g^{(1)}, e^{\mathcal{L}_0\tau} ([H_g^{(1)}, \rho_m \otimes \rho_c^0])]\}, \quad (\text{B.28})$$

and

$$\mathcal{L}_m^{(2)} \rho_m = - \int_0^\infty d\tau \text{Tr}_c\{[H_g^{(2)}, e^{\mathcal{L}_0\tau} ([H_g^{(2)}, \rho_m \otimes \rho_c^0])]\}. \quad (\text{B.29})$$

B.1.5 Simple perturbation theory

In deriving Eq. (B.26) we have so far only assumed that \tilde{g} is small compared to the typical frequency scales of the dynamics of the c_s mode. For now we will also assume that g_0 is small compared to δ and Δ_s . This allows us to neglect the term H'_g in \mathcal{L}_0 and the cavity correlation functions in Eqs. (B.28) and (B.29) can be evaluated in a straight forward manner. For the action of $\mathcal{L}_m^{(1)}$ we obtain

$$\mathcal{L}_m^{(1)} \rho_m = -i[\Lambda(B^\dagger B)^2, \rho_m] + \Gamma_\phi \mathcal{D}[B^\dagger B], \quad (\text{B.30})$$

where $\Lambda = \text{Im}\{S_{gg}^{(1)}(0)\}$, $\Gamma_\phi = \text{Re}\{S_{gg}^{(1)}(0)\}$ and

$$S_{gg}^{(1)}(\omega) = \tilde{g}^2 \int_0^\infty d\tau \text{Tr}_c \{c_s e^{\mathcal{L}_0 \tau} (c_s^\dagger \rho_c^0)\} e^{-i\omega\tau}. \quad (\text{B.31})$$

We find $S_{gg}^{(1)}(\omega) = \tilde{g}^2 / (-i(\Delta_s + \omega) + \kappa)$ and after inserting back the definition of \tilde{g} in the limit $|g_0\alpha/\delta| \ll 1$ we recover the expressions for Λ and Γ_ϕ given in Eq. (9) in the main text. Similarly we obtain

$$\mathcal{L}_m^{(2)} \rho_m = -i[\delta\omega_m^{(2)} B^\dagger B, \rho_m] + \frac{\gamma^{(2)}}{2} \mathcal{D}[B], \quad (\text{B.32})$$

where $\delta\omega_m^{(2)} = \text{Im}\{S_{gg}^{(2)}(\tilde{\omega}_m)\}$, $\gamma^{(2)} = \text{Re}\{S_{gg}^{(2)}(\tilde{\omega}_m)\}$ and

$$S_{gg}^{(2)}(\omega) = \frac{g_0^2 \sin^4(\theta)}{4} \int_0^\infty d\tau \text{Tr}_c \{c_s C e^{\mathcal{L}_0 \tau} (c_s^\dagger C^\dagger \rho_c^0)\} e^{-i\omega\tau}. \quad (\text{B.33})$$

The small frequency shift $\delta\omega_m^{(2)}$ can be absorbed into the definition of $\tilde{\omega}_m$ and, since $\gamma^{(2)} \approx \gamma' \sin^2(\theta) g_0^2 / (4\delta^2)$, for not too large mixing angles θ , $\gamma^{(2)}$ can always be neglected compared to γ' . All together the final effective phonon master equation is

$$\begin{aligned} \dot{\rho}_m = & -i[\tilde{\omega}_m B^\dagger B + \Lambda(B^\dagger B)^2, \rho_m] + \Gamma_\phi \mathcal{D}[B^\dagger B] \rho_m \\ & + \frac{\gamma}{2} \mathcal{D}_{\text{th}}[B] \rho_m + \frac{\gamma'}{2} \mathcal{D}[B] \rho_m, \end{aligned} \quad (\text{B.34})$$

which is the single resonator version of ME (8) given in the main text.

B.1.6 Corrections

Let us now extend the above result to the case where \tilde{g} is small compared to Δ_s and δ , but the bare interaction g_0 is not. In this case the general expressions in Eqs. (B.28) and (B.29) still apply, but the effect of H'_g must be taking into account when evaluating the correlation functions. To illustrate this, let us assume that g_0

is still small compared to δ . Then, by assuming that the C mode is initially in the ground state, we obtain approximately

$$H_{\text{lin}} + H'_g \approx -(\Delta_s - \Delta_B B^\dagger B) c_s^\dagger c_s, \quad (\text{B.35})$$

where the off-resonant frequency shift is

$$\Delta_B = \frac{g_0^2 \cos^4(\theta)}{4(\tilde{\Delta}_a + \tilde{\omega}_m - \Delta_s)}, \quad (\text{B.36})$$

and can be comparable to Δ_s . Therefore, we must evaluate the correlation function for each phonon number state $|n\rangle$ separately and write the resulting non-linear interaction as

$$\mathcal{L}_m^{(1)} \rho_m = \sum_n n^2 (-i [\Lambda(n) |n\rangle \langle n|, \rho_m] + \Gamma_\phi(n) \mathcal{D}[|n\rangle \langle n|]). \quad (\text{B.37})$$

Here $\Lambda(n)$ and $\Gamma_\phi(n)$ are the imaginary and real part of

$$S_{gg}^{(1)}(\omega = -n\Delta_B) = \frac{n^2 \tilde{g}^2}{-i(\Delta_s - n\Delta_B) + \kappa}. \quad (\text{B.38})$$

We see that in this parameter regime more complicated nonlinearities can occur, but the overall magnitude and the ratio between coherent and dephasing interactions remains the same. In principle, this analysis can be extended to the regime, where g_0 is comparable to δ . However, in this case no simple analytic expressions for $\lambda(n)$ and $\Gamma_\phi(n)$ can be derived and need to be evaluated numerically.

B.1.7 Numerical simulation

To assess the validity of the effective phonon ME we now compare our result with the dynamics of the full OMS. Since we are mainly interested in the relation between the phonon non-linearity and the corresponding dephasing and decay rates,

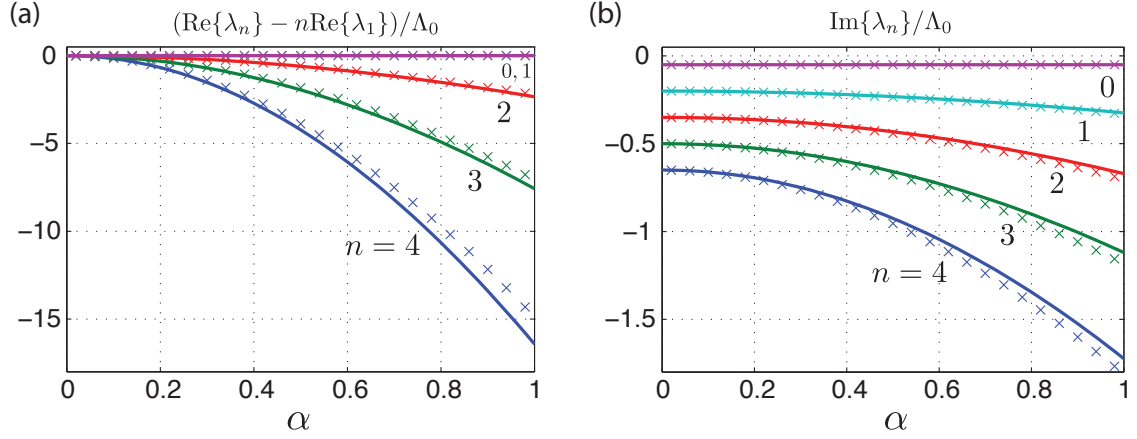


Figure B.1: Comparison of the effective analytic description (Eqs. (B.40), lines) with exact eigenvalues of the Hamiltonian in Eq. (B.39) (crosses) for different cavity field amplitudes α . All results are normalized to the scale $\Lambda_0 = g_0^4/(16|\Delta_s|\delta^2)$ of the non-linearity. (a) Deviation of the real parts of the eigenvalues from the result expected for a linear oscillator, such that the splitting of the curves indicates an effective non-linearity. (b) Imaginary parts of the eigenvalues corresponding to decays. In both plots we used the parameters $\Delta_s/g_0 = -1$, $\delta/g_0 = 5$, $\kappa/g_0 = 2.5 \times 10^{-2}$, $\gamma_m/g_0 = 2.5 \times 10^{-4}$ and $N_{\text{th}} = 1$.

it is sufficient to evaluate the spectrum of the non-Hermitian Hamiltonian, which for the full model it is given by

$$\tilde{H}_{\text{full}} = H_{\text{lin}} + H_g - i\kappa c_s^\dagger c_s - i\kappa c_a^\dagger c_a - i\frac{\gamma}{2}(N_{\text{th}} + 1)b^\dagger b - i\frac{\gamma}{2}N_{\text{th}}bb^\dagger. \quad (\text{B.39})$$

In Fig. B.1 we plot the real and imaginary parts of the lowest eigenvalues λ_n of \tilde{H}_{full} , which correspond to the lowest number states $|n\rangle$ of the B mode. From the effective phonon model given in Eq. (B.34) and (B.37) we obtain the approximate analytic results

$$\text{Re}\{\lambda_n\} = n\tilde{\omega}_m + n^2\Lambda(n), \quad (\text{B.40a})$$

and

$$|\text{Im}\{\lambda_n\}| = \frac{\gamma}{2}N_{\text{th}} + n\left(\frac{\gamma}{2}(2N_{\text{th}} + 1) + \frac{\gamma'}{2}\right) + n^2\Gamma_\phi(n). \quad (\text{B.40b})$$

We see a good agreement between these results for the effective model and the exact numerics, both for the real and imaginary parts. Although there are some deviations due to higher-order effects, the effective non-linear splitting (Fig. B.1(a)) is much larger than the induced decoherence (Fig. B.1(b)), as is expected for the chosen parameters. Hence, we conclude that the effective model accurately describes the dynamics of the mechanical resonator, and that the effective phonon non-linearity may serve as a basis for gate operations as discussed in the main text and in the following section.

B.2 Phonon-phonon interactions

The derivation of the effective phonon nonlinearity, as outlined above for a single resonator, can be easily adapted to two resonators as discussed in the main text. In this case we have

$$H_0 = \sum_{i=1,2} \omega_m^i b_i^\dagger b_i - \Delta_s c_s^\dagger c_s - \Delta_a c_a^\dagger c_a, \quad (\text{B.41})$$

and

$$H_g = \frac{g_0}{2} \left[c_a c_s^\dagger (b_1^\dagger - b_2^\dagger) + c_a^\dagger c_s (b_1 - b_2) \right]. \quad (\text{B.42})$$

After changing into the displaced representation to eliminate the driving field we obtain the linearized Hamiltonian

$$H_{\text{lin}} = H_0 + \sqrt{2} \left(G(t) c_a b_a^\dagger + G^*(t) c_a^\dagger b_a \right), \quad (\text{B.43})$$

where $b_a = (b_1 - b_2)/\sqrt{2}$ and $G(t) = g_0 \alpha(t)/2$. For similar mechanical frequencies $\omega_m^1 \simeq \omega_m^2 = \omega_m$ the symmetric resonator mode is decoupled and we can simply repeat the analysis from above by identifying $b \equiv b_a$ and replacing g_0 by $\sqrt{2}g_0$.

For arbitrary ω_i , we write the linear part of the Hamiltonian in its diagonal form

$$H_{\text{lin}} = -\Delta_s c_s^\dagger c_s - \tilde{\Delta}_a C^\dagger C + \tilde{\omega}_1 B_1^\dagger B_1 + \tilde{\omega}_2 B_2^\dagger B_2. \quad (\text{B.44})$$

As in the single-resonator case the c_s mode is unaffected, but the c_a mode now couples to both b_1 and b_2 . The resulting hybridized modes C , B_\pm depend on the choice of parameters $\omega_m^{1,2}$, Δ_a and G . For the case of interest, i.e. for a symmetric detuning $\omega_m^{1,2} = -\Delta_a \mp \delta$, we obtain

$$C = \cos(2\Theta)c_a - \sin(2\Theta)(B_1 + B_2)/\sqrt{2}, \quad (\text{B.45})$$

$$B_1 = \cos^2(\Theta)b_1 + \sin(2\Theta)c_a/\sqrt{2} - \sin^2(\Theta)b_2, \quad (\text{B.46})$$

$$B_2 = \cos^2(\Theta)b_2 + \sin(2\Theta)c_a/\sqrt{2} - \sin^2(\Theta)b_1, \quad (\text{B.47})$$

where $\tan(2\Theta) = -\sqrt{2}|G|/\delta$. Therefore, for small Θ the modes $B_{1,2}$ correspond to the original mechanical resonator modes $b_{1,2}$ and $\tilde{\omega}_i \approx \omega_m^i$.

As above, we can now re-express the dissipation and the non-linear coupling H_g in terms of C and B_\pm . The modified mechanical dissipation terms are given

$$\tilde{\mathcal{L}}_\gamma = \sum_{i=1,2} \frac{\gamma}{2} \cos^2(2\Theta) \mathcal{D}_{\text{th}}[B_i] + \frac{\kappa}{2} \sin^2(2\Theta) \mathcal{D}[B_i], \quad (\text{B.48})$$

and for small Θ the optical decay rate $\gamma' = \kappa \sin^2(2\Theta)$ is the same as given above and in the main text. Using the decomposition of the non-linear coupling as done in Eq. (B.15), we obtain

$$H_g^{(1)} = \frac{g_0}{\sqrt{8}} \sin(2\Theta) (c_s + c_s^\dagger) (B_1^\dagger B_1 - B_2^\dagger B_2), \quad (\text{B.49})$$

the contribution $H_g^{(2)}$ vanishes and

$$H_g' = \frac{g_0}{2} \cos(2\Theta) (C c_s^\dagger (B_1^\dagger - B_2^\dagger) + \text{H.c.}). \quad (\text{B.50})$$

We see that the structure and also the relative frequency scales are identical to the corresponding terms discussed for the single resonator above. Therefore, under the same conditions we can eliminate the cavity mode and obtain the effective phonon master equation

$$\begin{aligned} \dot{\rho}_m = & -i \left[\sum_i \tilde{\omega}_i B_i^\dagger B_i + \Lambda (B_1^\dagger B_1 - B_2^\dagger B_2)^2, \rho_m \right] \\ & + \Gamma_\phi \mathcal{D}[(B_1^\dagger B_1 - B_2^\dagger B_2)] \rho_m + \tilde{\mathcal{L}}_\gamma \rho_m. \end{aligned} \quad (\text{B.51})$$

For small Θ this equation reduces to ME (8) in the main text and higher-order corrections can be included in the same way as discussed for the single resonator case.

Bibliography

- [1] U Akram, N Kiesel, M Aspelmeyer, and G J Milburn. Single-photon optomechanics in the strong coupling regime. *New Journal of Physics*, 12(8):083030, 2010.
- [2] O. Arcizet, P.-F. Cohadon, T. Briant, M. Pinard, and A. Heidmann. Radiation-pressure cooling and optomechanical instability of a micromirror. *Nature*, 444:71–74, 2006.
- [3] Markus Aspelmeyer and Keith Schwab. Focus on mechanical systems at the quantum limit. *New Journal of Physics*, 10(9):095001, 2008.
- [4] S Basiri-Esfahani, U Akram, and G J Milburn. Phonon number measurements using single photon opto-mechanics. *New Journal of Physics*, 14(8):085017, 2012.
- [5] J Borregaard, P. Kómár, E. M. Kessler, M. D. Lukin, and A. S. Sørensen. Long-distance entanglement distribution using individual atoms in optical cavities. *Physical Review A*, 92(1):012307, July 2015.
- [6] J. Borregaard, P. Kómár, E. M. Kessler, A. S. Sørensen, and M. D. Lukin. Heralded quantum gates with integrated error detection in optical cavities. *Physical Review Letters*, 114(March):110502, 2015.
- [7] R. J. Brecha, P. R. Rice, and M. Xiao. n two-level atoms in a driven optical cavity: Quantum dynamics of forward photon scattering for weak incident fields. *Phys. Rev. A*, 59:2392–2417, Mar 1999.
- [8] Ferdinand Brennecke, Stephan Ritter, Tobias Donner, and Tilman Esslinger. Cavity optomechanics with a bose-einstein condensate. *Science*, 322(5899):235–238, 2008.
- [9] H.J. Carmichael, R.J. Brecha, and P.R. Rice. Quantum interference and collapse of the wavefunction in cavity {QED}. *Optics Communications*, 82(12):73 – 79, 1991.

-
- [10] Tal Carmon and Kerry J. Vahala. Modal spectroscopy of optoexcited vibrations of a micron-scale on-chip resonator at greater than 1 ghz frequency. *Phys. Rev. Lett.*, 98:123901, Mar 2007.
 - [11] Jasper Chan, T. P. Mayer Alegre, Amir H. Safavi-Naeini, Jeff T. Hill, Alex Krause, Simon Gröblacher, Markus Aspelmeyer, and Oskar Painter. Laser cooling of a nanomechanical oscillator into its quantum ground state. *Nature*, 478:89–92, 2011.
 - [12] Jasper Chan, Amir H. Safavi-Naeini, Jeff T. Hill, Sen Meenehan, and Oskar Painter. Optimized optomechanical crystal cavity with acoustic radiation shield. *Applied Physics Letters*, 101(8):081115, 2012.
 - [13] D E Chang, A H Safavi-Naeini, M Hafezi, and O Painter. Slowing and stopping light using an optomechanical crystal array. *New Journal of Physics*, 13(2):023003, 2011.
 - [14] Darrick E. Chang, Anders S. Sørensen, Eugene A. Demler, and Mikhail D. Lukin. A single-photon transistor using nanoscale surface plasmons. *Nature Physics*, 3:807–812, 2007.
 - [15] H. K. Cheung and C. K. Law. Nonadiabatic optomechanical hamiltonian of a moving dielectric membrane in a cavity. *Phys. Rev. A*, 84:023812, Aug 2011.
 - [16] Thomas Corbitt, Christopher Wipf, Timothy Bodiya, David Ottaway, Daniel Sigg, Nicolas Smith, Stanley Whitcomb, and Nergis Mavalvala. Optical dilution and feedback cooling of a gram-scale oscillator to 6.9 mk. *Phys. Rev. Lett.*, 99:160801, Oct 2007.
 - [17] Marcelo Davanço, Jasper Chan, Amir H. Safavi-Naeini, Oskar Painter, and Kartik Srinivasan. Slot-mode-coupled optomechanical crystals. *Opt. Express*, 20(22):24394–24410, Oct 2012.
 - [18] L. Ding, C. Baker, P. Senellart, A. Lemaitre, S. Ducci, G. Leo, and I. Favero. Wavelength-sized gaas optomechanical resonators with gigahertz frequency. *Applied Physics Letters*, 98(11):113108, 2011.
 - [19] J. M. Dobrindt and T. J. Kippenberg. Theoretical analysis of mechanical displacement measurement using a multiple cavity mode transducer. *Phys. Rev. Lett.*, 104:033901, Jan 2010.
 - [20] L.-M. Duan and H. J. Kimble. Scalable photonic quantum computation through cavity-assisted interactions. *Phys. Rev. Lett.*, 92:127902, Mar 2004.
 - [21] Matt Eichenfield, Jasper Chan, Ryan M. Camacho, Kerry J. Vahala, and Oskar Painter. Optomechanical crystals. *Nature*, 462:78–82, 2009.

- [22] Ivan Favero and Khaled Karrai. Optomechanics of deformable optical cavities. *Nature Photonics*, 3:201–205, 2009.
- [23] Victor Fiore, Yong Yang, Mark C. Kuzyk, Russell Barbour, Lin Tian, and Hailin Wang. Storing optical information as a mechanical excitation in a silica optomechanical resonator. *Phys. Rev. Lett.*, 107:133601, Sep 2011.
- [24] C. Gardiner and P. Zoller. *Quantum Noise*. Springer, 2004.
- [25] C. Genes, A. Mari, D. Vitali, and P. Tombesi. Chapter 2 quantum effects in optomechanical systems. In *Advances in Atomic Molecular and Optical Physics*, volume 57 of *Advances In Atomic, Molecular, and Optical Physics*, pages 33 – 86. Academic Press, 2009.
- [26] S. Gigan, H. R. Bhm, M. Paternostro, F. Blaser, G. Langer, J. B. Hertzberg, K. C. Schwab, D. Buerle, M. Aspelmeyer, and A. Zeilinger. Self-cooling of a micromirror by radiation pressure. *Nature*, 444:67–70, 2006.
- [27] Simon Gröblacher, Klemens Hammerer, Michael R. Vanner, and Markus Aspelmeyer. Observation of strong coupling between a micromechanical resonator and an optical cavity field. *Nature*, 460:724–727, 2009.
- [28] Ivan S. Grudinin, Hansuek Lee, O. Painter, and Kerry J. Vahala. Phonon laser action in a tunable two-level system. *Phys. Rev. Lett.*, 104:083901, Feb 2010.
- [29] Subhadeep Gupta, Kevin L. Moore, Kater W. Murch, and Dan M. Stamper-Kurn. Cavity nonlinear optics at low photon numbers from collective atomic motion. *Phys. Rev. Lett.*, 99:213601, Nov 2007.
- [30] Jeff T. Hill, Amir H. Safavi-Naeini, Jasper Chan, and Oskar Painter. Coherent optical wavelength conversion via cavity optomechanics. *Nature Communications*, 3:1196, 2012.
- [31] E. M. Kessler, P. Kómár, M. Bishof, L. Jiang, a. S. Sørensen, J. Ye, and M. D. Lukin. Heisenberg-limited atom clocks based on entangled qubits. *Physical Review Letters*, 112(May):190403, 2014.
- [32] T. J. Kippenberg and K. J. Vahala. Cavity optomechanics: Back-action at the mesoscale. *Science*, 321(5893):1172–1176, 2008.
- [33] Dustin Kleckner and Dirk Bouwmeester. Sub-kelvin optical cooling of a micromechanical resonator. *Nature*, 444:75–78, 2006.
- [34] P. Kómár, E. M. Kessler, M. Bishof, L. Jiang, a. S. Sørensen, J. Ye, and M. D. Lukin. A quantum network of clocks. *Nature Physics*, 10(June):582–587, 2014.

- [35] Andreas Kronwald, Max Ludwig, and Florian Marquardt. Full photon statistics of a light beam transmitted through an optomechanical system. *Phys. Rev. A*, 87:013847, Jan 2013.
- [36] Jie-Qiao Liao and C. K. Law. Correlated two-photon scattering in cavity optomechanics. *Phys. Rev. A*, 87:043809, Apr 2013.
- [37] Max Ludwig, Björn Kubala, and Florian Marquardt. The optomechanical instability in the quantum regime. *New Journal of Physics*, 10(9):095013, 2008.
- [38] Max Ludwig, Amir H. Safavi-Naeini, Oskar Painter, and Florian Marquardt. Enhanced quantum nonlinearities in a two-mode optomechanical system. *Phys. Rev. Lett.*, 109:063601, Aug 2012.
- [39] M. D. Lukin. *Colloquium* : Trapping and manipulating photon states in atomic ensembles. *Rev. Mod. Phys.*, 75:457–472, Apr 2003.
- [40] Florian Marquardt, Joe P. Chen, A. A. Clerk, and S. M. Girvin. Quantum theory of cavity-assisted sideband cooling of mechanical motion. *Phys. Rev. Lett.*, 99:093902, Aug 2007.
- [41] Florian Marquardt and Steven M. Girvin. Trend: Optomechanics. *Physics*, 2:40, 2009.
- [42] William Marshall, Christoph Simon, Roger Penrose, and Dik Bouwmeester. Towards quantum superpositions of a mirror. *Phys. Rev. Lett.*, 91:130401, Sep 2003.
- [43] Constanze Hühberger Metzger and Khaled Karrai. Cavity cooling of a microlever. *Nature*, 432:1002–1005, 2004.
- [44] Haixing Miao, Stefan Danilishin, Thomas Corbitt, and Yanbei Chen. Standard quantum limit for probing mechanical energy quantization. *Phys. Rev. Lett.*, 103:100402, Sep 2009.
- [45] M. Notomi, E. Kuramochi, and H. Taniyama. Ultrahigh-q nanocavity with 1d photonic gap. *Opt. Express*, 16(15):11095–11102, Jul 2008.
- [46] A. Nunnenkamp, K. Børkje, and S. M. Girvin. Single-photon optomechanics. *Phys. Rev. Lett.*, 107:063602, Aug 2011.
- [47] A. D. O’Connell, M. Hofheinz, M. Ansmann, Radosław C. Bialczak, M. Lenander, Erik Lucero, M. Neeley, D. Sank, H. Wang, M. Weides, J. Wenner, John M. Martinis, and A. N. Cleland. Quantum ground state and single-phonon control of a mechanical resonator. *Nature*, 464:697–703, 2010.

- [48] T. P. Purdy, D. W. C. Brooks, T. Botter, N. Brahms, Z.-Y. Ma, and D. M. Stamper-Kurn. Tunable cavity optomechanics with ultracold atoms. *Phys. Rev. Lett.*, 105:133602, Sep 2010.
- [49] P. Rabl. Photon blockade effect in optomechanical systems. *Phys. Rev. Lett.*, 107:063601, Aug 2011.
- [50] J. M. Raimond, M. Brune, and S. Haroche. Manipulating quantum entanglement with atoms and photons in a cavity. *Rev. Mod. Phys.*, 73:565–582, Aug 2001.
- [51] C A Regal and K W Lehnert. From cavity electromechanics to cavity optomechanics. *Journal of Physics: Conference Series*, 264(1):012025, 2011.
- [52] P.R. Rice and H.J. Carmichael. Single-atom cavity-enhanced absorption. i. photon statistics in the bad-cavity limit. *Quantum Electronics, IEEE Journal of*, 24(7):1351–1366, Jul 1988.
- [53] Jacob T. Robinson, Christina Manolatou, Long Chen, and Michal Lipson. Ultrasmall mode volumes in dielectric optical microcavities. *Phys. Rev. Lett.*, 95:143901, Sep 2005.
- [54] A. H. Safavi-Naeini, T. P. Mayer Alegre, J. Chan, M. Eichenfield, M. Winger, Q. Lin, J. T. Hill, D. E. Chang, and O. Painter. Electromagnetically induced transparency and slow light with optomechanics. *Nature*, 472:69–73, 2011.
- [55] Amir H Safavi-Naeini and Oskar Painter. Proposal for an optomechanical traveling wave phononphoton translator. *New Journal of Physics*, 13(1):013017, 2011.
- [56] A. Schliesser, R. Rivière, G. Anetsberger, O. Arcizet, and T. J. Kippenberg. Resolved-sideband cooling of a micromechanical oscillator. *Nature Physics*, 4:415–419, 2008.
- [57] Michael Schmidt, Max Ludwig, and Florian Marquardt. Optomechanical circuits for nanomechanical continuous variable quantum state processing. *New Journal of Physics*, 14(12):125005, 2012.
- [58] R. J. Schoelkopf and S. M. Girvin. Wiring up quantum systems. *Nature*, 451:664–669, 2008.
- [59] Dan M. Stamper-Kurn. Cavity optomechanics with cold atoms. page arXiv:1204.4351, 2012.
- [60] K. Stannigel, P. Komar, S. J. M. Habraken, S. D. Bennett, M. D. Lukin, P. Zoller, and P. Rabl. Optomechanical quantum information processing with photons and phonons. *Phys. Rev. Lett.*, 109:013603, Jul 2012.

- [61] K. Stannigel, P. Rabl, A. S. Sørensen, P. Zoller, and M. D. Lukin. Optomechanical transducers for long-distance quantum communication. *Phys. Rev. Lett.*, 105:220501, Nov 2010.
- [62] Y. Tanaka, T. Asano, and S. Noda. Design of photonic crystal nanocavity with q -factor of $\sim 10^9$. *Lightwave Technology, Journal of*, 26(11):1532–1539, June 2008.
- [63] J. M. Taylor, A. S. Sørensen, C. M. Marcus, and E. S. Polzik. Laser cooling and optical detection of excitations in a lc electrical circuit. *Phys. Rev. Lett.*, 107:273601, Dec 2011.
- [64] J. D. Teufel, T. Donner, Dale Li, J. W. Harlow, M. S. Allman, K. Cicak, A. J. Sirois, J. D. Whittaker, K. W. Lehnert, and R. W. Simmonds. Sideband cooling of micromechanical motion to the quantum ground state. *Nature*, 475:359–363, 2011.
- [65] J. D. Teufel, Dale Li, M. S. Allman, K. Cicak, A. J. Sirois, J. D. Whittaker, and R. W. Simmonds. Circuit cavity electromechanics in the strong-coupling regime. *Nature*, 471:204–208, 2011.
- [66] J. D. Thompson, B. M. Zwickl, A. M. Jayich, Florian Marquardt, S. M. Girvin, and J. G. E. Harris. Strong dispersive coupling of a high-finesse cavity to a micromechanical membrane. *Nature*, 452:72–75, 2007.
- [67] E. Verhagen, S. Deléglise, S. Weis, A. Schliesser, and T. J. Kippenberg. Quantum-coherent coupling of a mechanical oscillator to an optical cavity mode. *Nature*, 482:63–67, 2012.
- [68] Stefan Weis, Rmi Rivire, Samuel Delglise, Emanuel Gavartin, Olivier Arcizet, Albert Schliesser, and Tobias J. Kippenberg. Optomechanically induced transparency. *Science*, 330(6010):1520–1523, 2010.
- [69] D. J. Wilson, C. A. Regal, S. B. Papp, and H. J. Kimble. Cavity optomechanics with stoichiometric sin films. *Phys. Rev. Lett.*, 103:207204, Nov 2009.
- [70] I. Wilson-Rae, N. Nooshi, W. Zwerger, and T. J. Kippenberg. Theory of ground state cooling of a mechanical oscillator using dynamical backaction. *Phys. Rev. Lett.*, 99:093901, Aug 2007.
- [71] Chi Xiong, Wolfram H P Pernice, Xiankai Sun, Carsten Schuck, King Y Fong, and Hong X Tang. Aluminum nitride as a new material for chip-scale optomechanics and nonlinear optics. *New Journal of Physics*, 14(9):095014, 2012.
- [72] Jing Zhang, Kunchi Peng, and Samuel L. Braunstein. Quantum-state transfer from light to macroscopic oscillators. *Phys. Rev. A*, 68:013808, Jul 2003.

-
- [73] Mian Zhang, Gustavo S. Wiederhecker, Sasikanth Manipatruni, Arthur Barnard, Paul McEuen, and Michal Lipson. Synchronization of micromechanical oscillators using light. *Phys. Rev. Lett.*, 109:233906, Dec 2012.